



Nonequilibrium Gas-Surface Interactions at High Temperature

**Thomas Schwartzentruer
REGENTS OF THE UNIVERSITY OF MINNESOTA**

**06/16/2020
Final Report**

DISTRIBUTION A: Distribution approved for public release.

**Air Force Research Laboratory
AF Office Of Scientific Research (AFOSR)/ RTA1
Arlington, Virginia 22203
Air Force Materiel Command**

DISTRIBUTION A: Distribution approved for public release.

REPORT DOCUMENTATION PAGE		<i>Form Approved</i> <i>OMB No. 0704-0188</i>	
<p>The public reporting burden for this collection of information is estimated to average 1 hour per response, including the time for reviewing instructions, searching existing data sources, gathering and maintaining the data needed, and completing and reviewing the collection of information. Send comments regarding this burden estimate or any other aspect of this collection of information, including suggestions for reducing the burden, to Department of Defense, Executive Services, Directorate (0704-0188). Respondents should be aware that notwithstanding any other provision of law, no person shall be subject to any penalty for failing to comply with a collection of information if it does not display a currently valid OMB control number.</p> <p>PLEASE DO NOT RETURN YOUR FORM TO THE ABOVE ORGANIZATION.</p>			
1. REPORT DATE (DD-MM-YYYY) 07-07-2020	2. REPORT TYPE Final Performance	3. DATES COVERED (From - To) 15 Mar 2017 to 14 Mar 2020	
4. TITLE AND SUBTITLE Nonequilibrium Gas-Surface Interactions at High Temperature		5a. CONTRACT NUMBER	
		5b. GRANT NUMBER FA9550-17-1-0057	
		5c. PROGRAM ELEMENT NUMBER 61102F	
6. AUTHOR(S) Thomas Schwartzentruber		5d. PROJECT NUMBER	
		5e. TASK NUMBER	
		5f. WORK UNIT NUMBER	
7. PERFORMING ORGANIZATION NAME(S) AND ADDRESS(ES) REGENTS OF THE UNIVERSITY OF MINNESOTA 200 OAK ST SE 224 MINNEAPOLIS, MN 55455-2009 US		8. PERFORMING ORGANIZATION REPORT NUMBER	
9. SPONSORING/MONITORING AGENCY NAME(S) AND ADDRESS(ES) AF Office of Scientific Research 875 N. Randolph St. Room 3112 Arlington, VA 22203		10. SPONSOR/MONITOR'S ACRONYM(S) AFRL/AFOSR RTA1	
		11. SPONSOR/MONITOR'S REPORT NUMBER(S) AFRL-AFOSR-VA-TR-2020-0083	
12. DISTRIBUTION/AVAILABILITY STATEMENT A DISTRIBUTION UNLIMITED: PB Public Release			
13. SUPPLEMENTARY NOTES			
14. ABSTRACT <p>Hypersonic vehicles generate extreme conditions in the thin shock-layer next to the vehicle surface, in which gas temperatures can exceed 10,000K. This creates high heat fluxes that the thermal protection system (TPS) must withstand. Additionally, the TPS may lose mass due to chemical reactions with dissociated oxygen present in the high-temperature boundary layer. This process, called ablation, involves coupled gas-phase, gas-surface, and material response physics. Since no single ground experiment can fully reproduce flight conditions, computational fluid dynamics (CFD) modeling of ablation is crucial for vehicle design and survivability. However, significant challenges remain in developing accurate ablation models. Such challenges include determining how TPS microstructure influences ablation rates, how the many individual model parameters can be determined while only macroscopic data (recession rates) are available from most ablation experiments, and how to accurately characterize the flow conditions in ablation testing facilities so that quantitative CFD validation studies can be performed. We propose to address these challenges by (1) fabricating new TPS samples and coatings including microstructure characterization along with direct simulation of microstructure reactions with boundary-layer gases, (2) using molecular beam experiments to determine individual gas-surface reaction rates, and (3) applying advanced CFD simulations. The project will focus on a variety of carbon-based TPS and ceramic TPS materials. In addition, new TPS samples with advanced ceramic coatings will be fabricated and tested as part of the project. This abstract is publicly releasable.</p>			
15. SUBJECT TERMS ablation, SiC passive and active oxidation, X-ray micro-tomography DSMC			

16. SECURITY CLASSIFICATION OF:			17. LIMITATION OF ABSTRACT	18. NUMBER OF PAGES	19a. NAME OF RESPONSIBLE PERSON
a. REPORT	b. ABSTRACT	c. THIS PAGE			19b. TELEPHONE NUMBER <i>(Include area code)</i>
Unclassified	Unclassified	Unclassified	UU		LEYVA, IVETT
					703-696-8478

FINAL GRANT REPORT

June 12th, 2020

FA9550-17-1-0057 – Gas Surface Interactions at High Temperature

Dr. Ivett Leyva: High-Speed Aerodynamics
Dr. Ali Sayir: Aerospace Materials for Extreme Environments

by
Thomas E. Schwartzenruber
Professor
Aerospace Engineering and Mechanics,
University of Minnesota

Phone: 612-625-6027

Fax: 612-626-1558

Email: schwart@umn.edu

Co-PIs: Prof. Graham Candler (Minnesota), Prof. Tim Minton (Montana State), Prof. Erica Corral (Arizona), Prof. John Perepezko (Wisconsin)

CONTENTS	PAGE #
I CARBON ABLATION	
I.1 Background and Motivation	1
I.2 Previous Research on Carbon Ablation	2
I.3 New Molecular Beam Experiments for Carbon Ablation	3
I.4 New Molecular Beam Data and New Ablation Model	3
I.5 US3D CFD Simulations using the Air-Carbon Ablation Model	6
I.6 Ablation Model Validation with VKI Plasmatron Tests (On-Going)	8
I.7 Experimental Measurements of Microstructure Influence	9
I.8 C-C Experiments and Possible Model Extension	13
II SILICON CARBIDE (PASSIVE-ACTIVE TRANSITION AND T-JUMP)	
II.1 Background and Motivation	15
II.2 Molecular Beam Experiments on SiC with Thin Oxide Layer	15
II.3 Molecular Beam Experiments on SiC with Thicker Oxide Layer	21
III Mo-Si-B BASED COATINGS AND TESTING	
III.1 Background and Motivation	22
III.2 Summary of Mo-Si-B Based Alloy Experimental Campaigns	22
III.3 Mo-Si-B Based Coating on SiC – Torch Facility Testing	24
III.4 Characterization of Oxyacetylene Torch Flow Conditions	26
List of Publications and Presentations	28
References	31
APPENDIX (separate document): UW-Madison detailed grant report	

I CARBON ABLATION

I.1 Background and Motivation

No single ground-test facility can reproduce hypersonic flight conditions and flight experiments are time consuming and expensive. As a result, numerical simulations equipped with accurate physical models are essential for understanding hypersonic flight physics. This research focuses on carbon ablation under hypersonic flight conditions. Novel laboratory experiments and modeling approaches are combined to significantly increase the accuracy of hypersonic carbon ablation predictions.

The most widely used ablation models are the B' (equilibrium-based) model and the finite-rate models from Park. It is well known, that for many hypersonic flight conditions of interest, the gas-surface interaction is not close to equilibrium. Equilibrium based models (i.e. the B' model) predict an upper-limit for the gas-surface reactivity and therefore generally overpredict the carbon surface recession rate. Properly considering the finite-rate of gas-surface reactions is more accurate, however, this physical accuracy comes with a dramatic increase in complexity. Instead of using chemical equilibrium theory, many individual reaction mechanisms must be prescribed, along with reaction rates and model parameters for each reaction.

Currently, the most widely used finite-rate carbon ablation models are the Park models [1] for O atoms, O₂ molecules, and N atoms reacting with carbon to form CO and CN. Figure 1a shows the Park model for $O + C(s) \rightarrow CO$, and Fig. 1b shows the Park model for $N + C(s) \rightarrow CN$, compared to data inferred from various experiments. An advantage of the Park model is that the reaction mechanisms are modelled with standard Arrhenius expressions. For oxidation (Fig. 1a), the reaction probability is seen to monotonically increase with temperature, in general agreement with the data. However, looking closely in the 800K – 5000K temperature range, it is evident that the experimental data does not show a monotonic increase with temperature. Rather a clear maximum CO reaction probability is observed, and the reactivity actually decreases as temperature is increased further. The experimental data and new models described in this report, accurately capture this non-Arrhenius behavior. This behavior is a result of surface-coverage dependent reactions, which also introduce pressure dependence into the ablation model. For nitridation it is known that the Park model parameters result in an inaccurately high CN formation probability. Therefore, Figs. 1a and 1b provide the motivation to significantly improve carbon ablation models for use in CFD simulations.

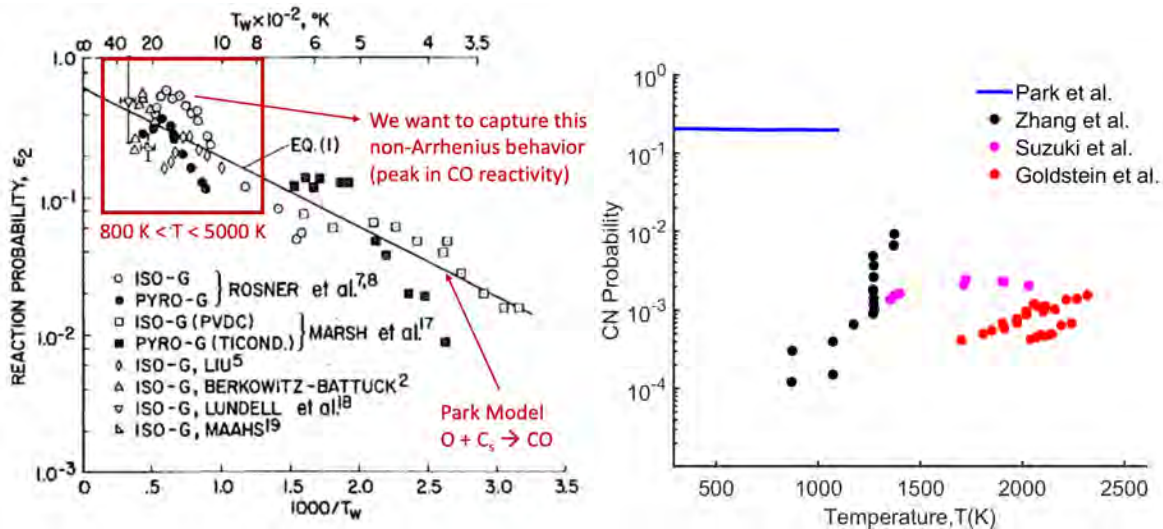


Figure 1: Reaction probability for (a) $O + C(s) \rightarrow CO$ and (b) $N + C(s) \rightarrow CN$ from the Park model compared to results inferred from various experiments. Figure 1a is taken and adapted from Ref. [1]. In Fig. 1b, Park et al. data is from Ref. [2], Zhang et al. data is from Ref. [3], Suzuki et al. data is from Ref. [4], and Goldstein et al. data is from Ref. [5].

I.2 Previous Research on Carbon Ablation

Two finite rate models that have been used in the recent literature include the Park model [1] and the Zhluktov and Abe (ZA) model [6]. Both models were used to compare computations to experimental data from the passive ablation nose-tip technology (PANT) configuration [7][8], and both models under-predicted the stagnation point ablative mass flux, under high pressure conditions. MacLean et al. [9] compared different models, two models based on the work of Park and two variants of the ZA model, and adjusted rate parameters to better match experimental data. Lewis et al. [10][11] performed a series of hypersonic ablation experiments in the X-2 facility at the University of Queensland, and CFD simulations comparing the Park and ZA models were performed by Alba et al. [12][13]. In these cases, the surface temperature ranged from 1770 to 2410 K. The predicted ablation products were quite different between the Park and ZA models, and neither of the models was able to predict the experimentally observed products, and further model parameter changes were proposed. A significant challenge in ablation modeling is that high enthalpy experiments (such as arc-jets or inductively coupled plasma (ICP) facilities) produce only macroscopic data such as surface recession and heat flux. Most often, this is insufficient data to determine individual reaction mechanisms and reaction rate parameters.

As part of a FY2010 AFOSR MURI project, new surface chemistry data was obtained using molecular beam gas-surface scattering experiments. The experiments were performed at Montana State University, and involved a pulsed beam of atomic and molecular oxygen, traveling at a nominal velocity of 7756 m/s, and impacting a vitreous carbon (VC) surface that was resistively heated to high temperatures. This hyperthermal beam was pulsed at a repetition rate of 2 Hz and was composed of 93% atomic and 7% molecular oxygen. The general experimental setup [14][15][16] includes a rotatable mass spectrometer to monitor both the incident molecular beam and the volatile species that scatter from the surface. At present, experiments have been performed for VC samples [14][17], highly oriented pyrolytic graphite (HOPG) samples [18], and FiberForm samples [19]. The experiments provide a wealth of data regarding what reactions are dominant and the reaction probabilities for different products leaving the surface. During the FY2010 MURI, such data was used to construct a probability model (for O atoms only) for use in direct simulation Monte Carlo (DSMC) [20] and a finite-rate model for use in computational fluid dynamics (CFD) [21].

The previous pulsed molecular beam experiments revealed **four general results** directly relevant to ablation processes under hypersonic conditions. **First**, reaction products scattered thermally (accommodated to the surface temperature), despite the high energy beam of reactants. This result implied that the beam energy and angle had no effect on the surface chemistry, rather, the beam simply acts as a supply of oxygen atoms to the surface and the material temperature is the dominant parameter controlling the reaction probability. **Second**, the rotatable mass spectrometer was able to clearly differentiate between individual reaction efficiencies. For example, CO was the dominant product at all temperatures, and CO₂ was a minor reaction product. **Third**, non-Arrhenius behavior was observed for the CO product formation. At temperatures between 800-1200 K, the probability of CO production increased with surface temperature. However, above approximately 1200 K, CO production was observed to decrease while the O atom flux leaving the surface markedly began to increase (indicating a decrease in surface coverage). Therefore, despite the low pressure environment (near-vacuum) of the molecular beam experiments, the collected data spanned regimes of high surface coverage and the transition to low surface coverage. **Fourth**, molecular beam experiments were performed on three types of carbon surfaces: highly-oriented pyrolytic graphite (HOPG) [18], vitreous carbon (VC) [14], and FiberForm [19]. The main trends discussed above were consistent across each material, indicating that the measurements were general to many ablating carbon materials. Each of these four key results supported the premise that molecular beam experiments may provide relevant data for modeling carbon ablation occurring in the presence of a hypersonic boundary layer.

However, certain assumptions were required in prior modeling efforts that led to some level of uncertainty in interpreting the experimental measurements and incorporating them in hypersonic ablation

models. Specifically, although reaction products scattered thermally, it could be possible that the high beam energy and low atomic oxygen flux, compared to that from a boundary layer gas, produces different surface chemistry than would be expected in an actual hypersonic boundary layer. Furthermore, the pulsed nature of the molecular beam led to in-depth studies of the time-varying aspects of the experiments [22][23], that added additional confusion. A good comparison of models prior to the current project is shown in Fig. 2 for the dominant reaction of $O + C(s) \rightarrow CO$ (note that Fig. 2 is taken directly from Ref. [22]). Here, the Park probability is seen to monotonically increase as temperature increases, the ZA model produces very little CO (but significant CO_2 instead), and the Alba correction to the ZA model results in substantial CO with an increasing trend. Furthermore, the MURI model (labelled as “PSMM”) predicts the peak in CO probability discussed earlier. In contrast, the model by Swaminathan-Gopalan et al. [22] (labelled as “current”), which was based on a specific reinterpretation of the molecular beam data, predicts that the carbon reactivity *decreases* as temperature is increased.

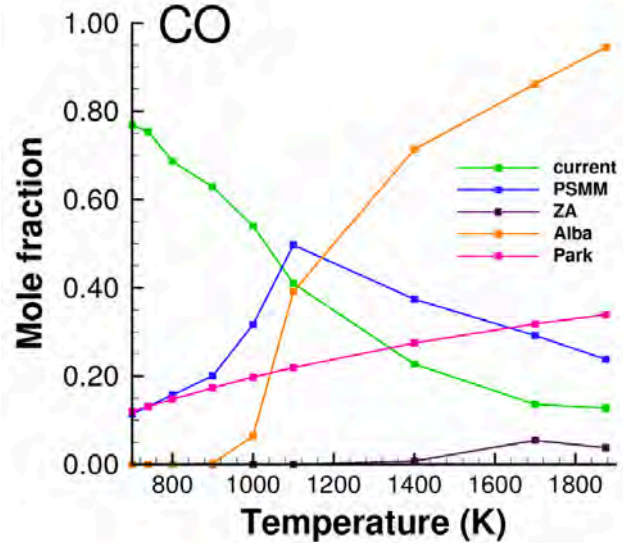


Figure 2: Comparison of various ablation models. Taken directly from Ref. [22].

I.3 New Molecular Beam Experiments for Carbon Ablation

To address these uncertainties, and to provide a larger set of experimental data, new molecular beam experiments were performed as part of this project. Full details are contained in Refs. [17,18,24]. Some new experiments involved continuous beams containing O or N atoms with incident velocities of approximately 2000 m/s, which were directed at a vitreous carbon (VC) surface at temperatures ranging from 800 – 1873 K. Furthermore, the incident O- or N-atom flux in the new experiments was up to three orders of magnitude higher than the fluxes used in the earlier studies with the pulsed beams. **Therefore, the new, continuous, lower velocity, and higher flux, molecular beam experiments were able to address the main assumptions and uncertainties from the previous pulsed beam experiments.** As described in detail in Ref. [22], despite significant differences between the new continuous beam experiments and earlier pulsed beam conditions, the results are remarkably similar. In fact, each of the four general results discussed above were also observed in the new experiments, and therefore, the new experiments corroborate the reaction mechanisms proposed during the MURI project as well as the original assumptions made in interpreting the molecular beam data [20][21]. Furthermore, the new experiments include exposure of VC samples to beams containing N and N_2 , and also revealed the probabilities of N-atom and O-atom surface recombination reactions to form gas-phase N_2 and O_2 molecules. Since complete data is now available for O atoms, N atoms, a mixture of O and N atoms, along with separate data on O_2 collisions with carbon [25][26][27], we have constructed an **air**-carbon ablation model for widespread use in CFD simulations under the current project.

I.4 New Molecular Beam Data and New Ablation Model

The results of the new molecular beam experiments are fully described in Ref. [24], and for brevity they are now presented along with the new model results. The new continuous molecular beam experiments expose a partially ablated, high temperature, VC carbon sample to a continuous flux of O or N atoms at velocities comparable to the mean thermal speed of atomic species in a hypersonic boundary layer (≈ 2000 m/s). Under such conditions, all reactions were observed to proceed thermally and products leave the surface accommodated to the carbon surface temperature. The rotatable mass spectrometer is able to

quantify the efficiencies of individual gas-surface interactions, both reactive and non-reactive, as a function of surface temperature. The results for O atoms interacting with carbon are shown by symbols in Fig. 3. Reactions forming CO (the dominant product) are surface-coverage dependent reactions that exhibit non-Arrhenius rate behavior at high surface temperature where surface coverage is reduced due to the desorption of O atoms (i.e. the decrease in CO-black coincides with an increase in O-blue). Reactions forming CO₂ (minor product) are found to reduce as temperature is increased and are not measurable above a certain threshold temperature. In addition to the oxidation reactions producing CO and CO₂, oxygen atoms are observed to recombine on the surface to produce gas-phase O₂ (green) with an efficiency that is lower than CO production, but not negligible.

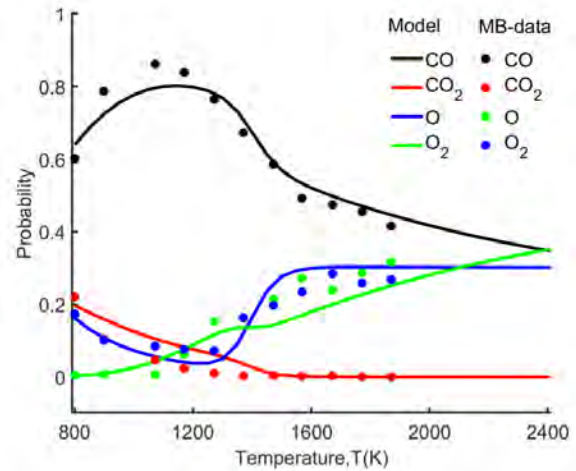


Figure 3: CO reaction probability due to O atoms.

Nitrogen atoms may recombine on the surface to produce gas-phase N₂ or react to produce CN. Importantly, as shown in Fig. 4, the molecular beam data indicated that the recombination efficiency of N atoms was more than an order of magnitude higher than the reaction efficiency to produce CN. This result was also inferred from ICP torch experiments at the University of Vermont (shown by the black and red triangles in Fig. 4 [28]). Also evident in Fig. 4 is the discrepancy in CN probability inferred from molecular beam experiments (very low effective pressure) compared to ICP experiments from Vermont and VKI [29] (where N atom partial pressures were approximately 1600 Pa). The new model captures pressure dependence through surface coverage changes, and as seen in Fig. 3, is able to capture the different trends in CN probability for both molecular beam and ICP conditions. Finally, preliminary experiments where molecular beams containing a *mixture* of N and O atoms interact with hot VC samples have been performed as part of this project [30], which provide valuable information about if, and how, N and O atoms compete for surface coverage and indirectly influence oxidation and nitridation reactions. Although not shown in this report, these measurements were crucial to construct the full air-carbon ablation model.

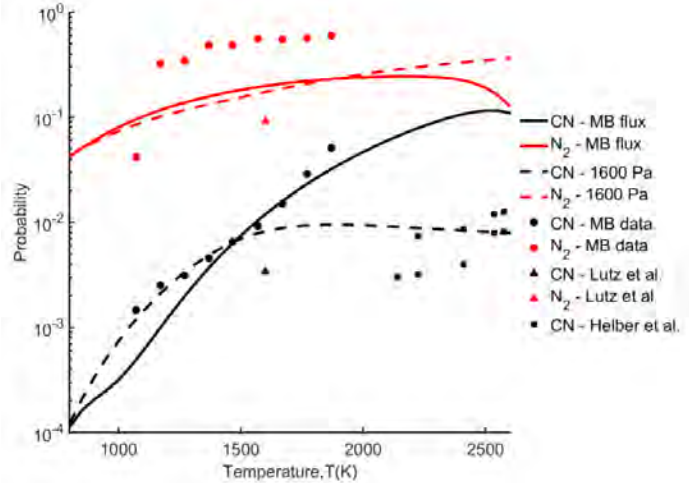


Figure 4: CN and N₂ reaction probability due to N atoms.

In addition to this wealth of new experimental data, additional molecular beam data for O₂ interacting with carbon has recently been reported [25]. Figure 5 combines this new data with a legacy experimental O₂

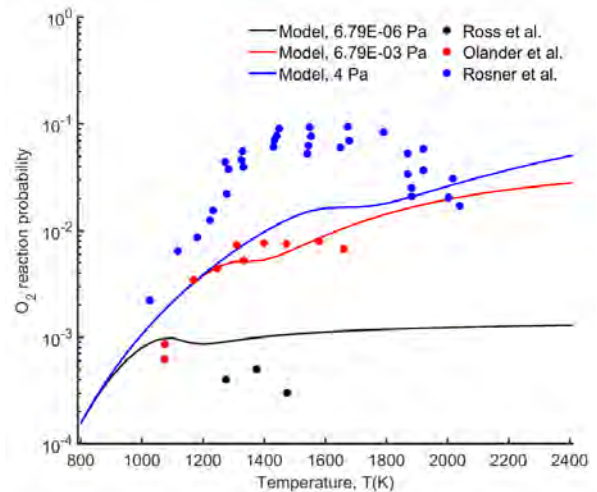


Figure 5: CO/CO₂ reaction probability due to O₂.

measurements [26][27], and plots the new model predictions. Again, the new model includes pressure dependence through surface coverage changes, and is able to predict the variations in both temperature and pressure evident from the data.

In summary, combining the consistent results of the original high-velocity pulsed molecular beam data with the new lower-velocity continuous beam data, we now have sufficient experimental data for oxygen and nitrogen interactions with carbon and we have extended the previous oxygen-carbon model [21] to a new finite-rate *air*-carbon ablation model. The model is shown in Table 1, and Ref. [30] contains complete details of the model formulation, including the rationale behind all 20 reaction mechanisms and model parameter values.

Table 1: Reaction mechanisms and rate parameters for new air-carbon ablation model

R.No	Reaction	Reaction Rate	Rate Constant	Units
1.	$O + (s) \rightarrow O(s)$	$k_{O1}[O][(s)]$	$\frac{F_O}{B} * 0.3$	$m^3 mol^{-1} s^{-1}$
2.	$O(s) \rightarrow O + (s)$	$k_{O2}[O(s)]$	$\frac{2\pi m_O k_b^2 T^2}{A_v B h^3} \exp \frac{-44277}{T}$	s^{-1}
3.	$O + O(s) + C(b) \rightarrow CO + O + (s)$	$k_{O3}[O][O(s)]$	$\frac{F_O}{B} 100 \exp \frac{-4000}{T}$	$m^3 mol^{-1} s^{-1}$
4.	$O + O(s) + C(b) \rightarrow CO_2 + (s)$	$k_{O4}[O][O(s)]$	$\frac{F_O}{B} \exp \frac{-500}{T}$	$m^3 mol^{-1} s^{-1}$
5.	$O + (s) \rightarrow O^*(s)$	$k_{O5}[O][(s)]$	$\frac{F_O}{B} * 0.7$	$m^3 mol^{-1} s^{-1}$
6.	$O^*(s) \rightarrow O + (s)$	$k_{O6}[O^*(s)]$	$\frac{2\pi m_O k_b^2 T^2}{A_v B h^3} \exp \frac{-96500}{T}$	s^{-1}
7.	$O + O^*(s) + C(b) \rightarrow CO + O + (s)$	$k_{O7}[O][O^*(s)]$	$\frac{F_O}{B} 1000 \exp \frac{-4000}{T}$	$m^3 mol^{-1} s^{-1}$
8.	$O^*(s) + O^*(s) \rightarrow O_2 + 2(s)$	$k_{O8}[O^*(s)]^2$	$\sqrt{\frac{A_v}{B}} F_{O,2D} * 1 * 10^{-3} \exp \frac{-15000}{T}$	$m^2 mol^{-1} s^{-1}$
9.	$O(s) + O(s) \rightarrow O_2 + 2(s)$	$k_{O9}[O(s)]^2$	$\sqrt{\frac{A_v}{B}} F_{O,2D} 5 * 10^{-5} \exp \frac{-15000}{T}$	$m^2 mol^{-1} s^{-1}$
10.	$N + (s) \rightarrow N(s)$	$k_{N1}[N][(s)]$	$\frac{F_N}{B} \exp \frac{-2500}{T}$	$m^3 mol^{-1} s^{-1}$
11.	$N(s) \rightarrow N + (s)$	$k_{N2}[N(s)]$	$\frac{2\pi m_N k_b^2 T^2}{A_v B h^3} \exp \frac{-73971}{T}$	s^{-1}
12.	$N + N(s) + C(b) \rightarrow CN + N + (s)$	$k_{N3}[N][N(s)]$	$\frac{F_N}{B} 1.5 \exp \frac{-7000}{T}$	$m^3 mol^{-1} s^{-1}$
13.	$N + N(s) \rightarrow N_2 + (s)$	$k_{N4}[N][N(s)]$	$\frac{F_N}{B} 0.5 \exp \frac{-2000}{T}$	$m^3 mol^{-1} s^{-1}$
14.	$N(s) + N(s) \rightarrow N_2 + 2(s)$	$k_{N5}[N(s)]^2$	$\sqrt{\frac{A_v}{B}} F_{N,2D} 0.1 \exp \frac{-21000}{T}$	$m^2 mol^{-1} s^{-1}$
15.	$N(s) + C(b) \rightarrow CN + (s)$	$k_{N6}[N(s)]$	$1e + 08 \exp \frac{-20676}{T}$	s^{-1}
16.	$O_2 + 2(s) \rightarrow 2O(s)$	$k_{ox1}[O_2][(s)]^2$	$\frac{F_{O_2}}{B^2} 1 \exp \frac{-8000}{T}$	$m^5 mol^{-2} s^{-1}$
17.	$O_2 + O(s) + C(b) \rightarrow CO + O_2 + (s)$	$k_{ox2}[O_2][O(s)]$	$\frac{F_{O_2}}{B} 100 \exp \frac{-4000}{T}$	$m^3 mol^{-1} s^{-1}$
18.	$O_2 + O(s) + C(b) \rightarrow CO_2 + O + (s)$	$k_{ox3}[O_2][O(s)]$	$\frac{F_{O_2}}{B} 1 \exp \frac{-500}{T}$	$m^3 mol^{-1} s^{-1}$
19.	$O_2 + 2(s) \rightarrow 2O^*(s)$	$k_{ox4}[O_2][(s)]^2$	$\frac{F_{O_2}}{B^2} 1 \exp \frac{-8000}{T}$	$m^5 mol^{-2} s^{-1}$
20.	$O_2 + O^*(s) + C(b) \rightarrow CO + O_2 + (s)$	$k_{ox5}[O_2][O^*(s)]$	$\frac{F_{O_2}}{B} 1000 \exp \frac{-4000}{T}$	$m^3 mol^{-1} s^{-1}$

1.5 US3D CFD Simulations using the Air-Carbon Ablation Model

The new air-carbon ablation model has been implemented in the US3D CFD code. Although not described in this report, the implementation of such surface-coverage dependent models is not trivial, and considerations of efficiency and convergence are important.

An example US3D solution is shown in Fig. 6, corresponding to a 10 cm diameter sphere cone flying at 5 km/s and approximately 45 km altitude ($\rho = 1.65 \times 10^{-3} \text{ kg/m}^3$, $T = 227.2 \text{ K}$). The wall temperature is fixed to $T_w=1600 \text{ K}$. The temperature contours are shown in Fig. 6 (left), where the post-shock temperature is approximately 5500 K. Under these conditions, significant oxygen dissociation and little nitrogen dissociation is expected. The oxygen then reacts with the carbon surface to form mainly CO, which can be seen in Fig. 6 (right).

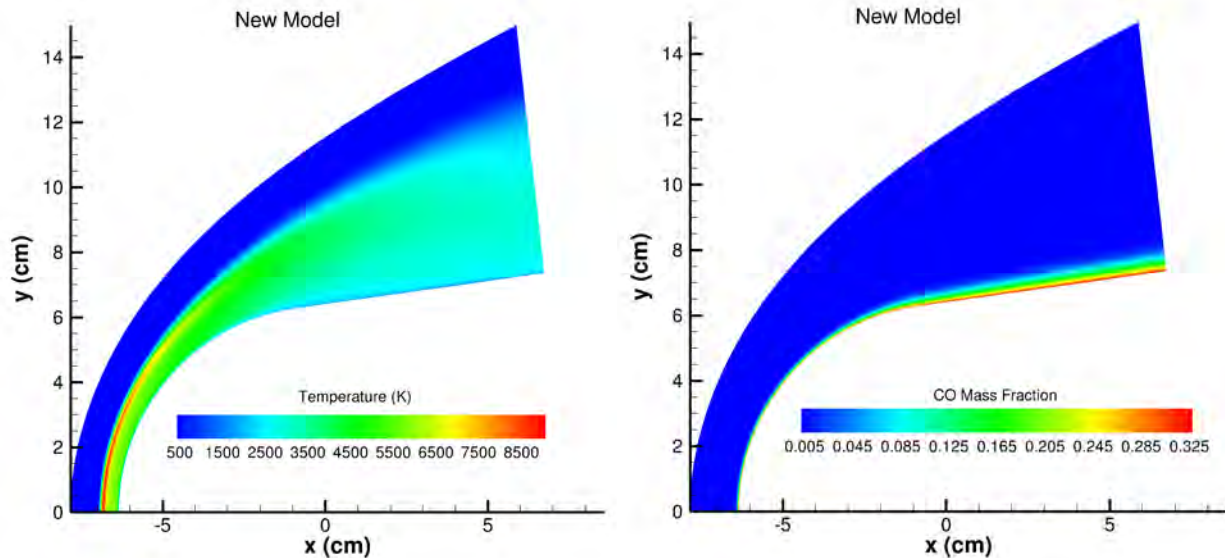


Figure 6: US3D CFD solutions for hypersonic flow over a sphere-cone geometry. Trans-rotational temperature contours (left) and CO mass fraction (right) are shown.

The results of the new air-carbon ablation model are compared with results from the O-carbon FY2010 MURI model [21] and the modified ZA model from MacLean et al. (ZAM [9]) in Figs. 7, 8, and 9, respectively. First, in Figs. 7a, 8a, and 9a (purple circles), the total mass loss rate at the stagnation point, which governs the net carbon recession rate, is seen to be $0.06 \text{ kg/(m}^2\text{s)}$ for both the new model and the MURI model, compared to $0.05 \text{ kg/(m}^2\text{s)}$ for the ZAM model. The new model and MURI models are expected to agree for cases dominated by oxygen dissociation, and it is promising that the predicted recession rate is close to the ZAM model since it has been validated with recession data from Arcjet tests [9]. However, in Fig. 9a, the ZAM model is seen to predict significant CO_2 production, comparable to the CO production. In contrast, the new model (Fig. 7a) shows purely CO production and little CO_2 production (as observed in molecular beam experiments). As a result, the ZAM model predicts noticeable CO_2 in the near-wall boundary layer (Fig. 9b), whereas the new model predicts entirely CO with only trace amounts of CO_2 (Fig. 7b). Finally, comparing the new model with the MURI model (in Figs. 7a,b and 8a,b), the new model is seen to predict that N atoms are consumed at the carbon surface and recombine into N_2 molecules. Recall that molecular beam experiments and ICP tests determined that the probability of N atom recombination was approximately ten times that of CN production.

The new air-carbon ablation model is implemented as a “plugin” to US3D. The example presented in this report is just one flight condition, however the new model is applicable over a wide range of temperature, pressure, and near surface gas composition. US3D users will be able to use this “plugin” and verify/validate the model for their specific conditions of interest. Model parameters are expected to need small adjustments as validation studies are performed by the community.

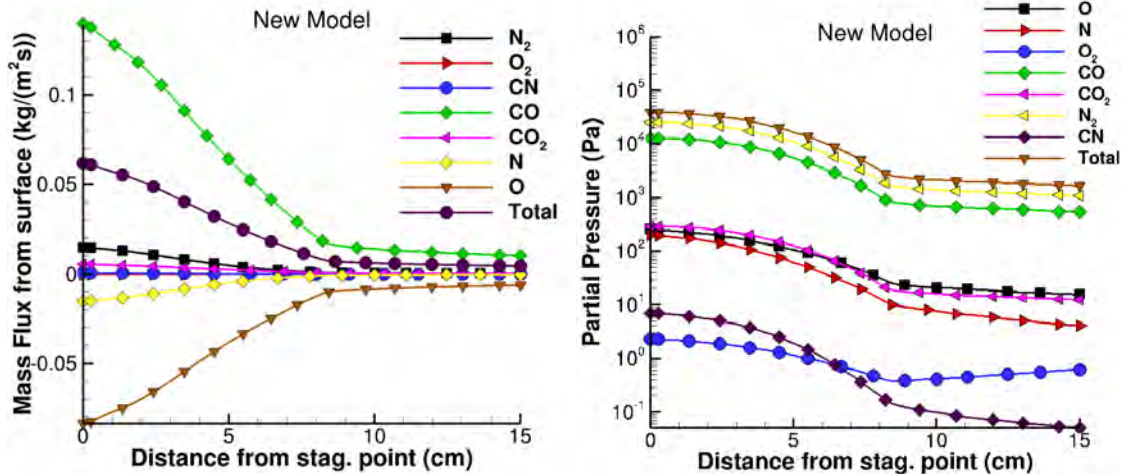


Figure 7: New model results for (a) mass flux off the surface and (b) near-wall composition.

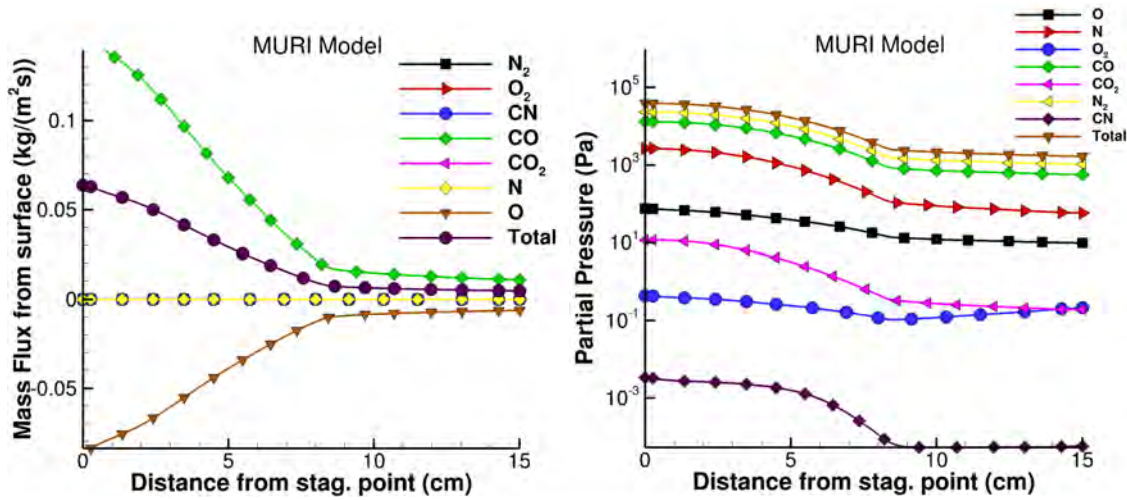


Figure 8: FY2010 MURI model results for (a) mass flux off the surface and (b) near-wall composition.

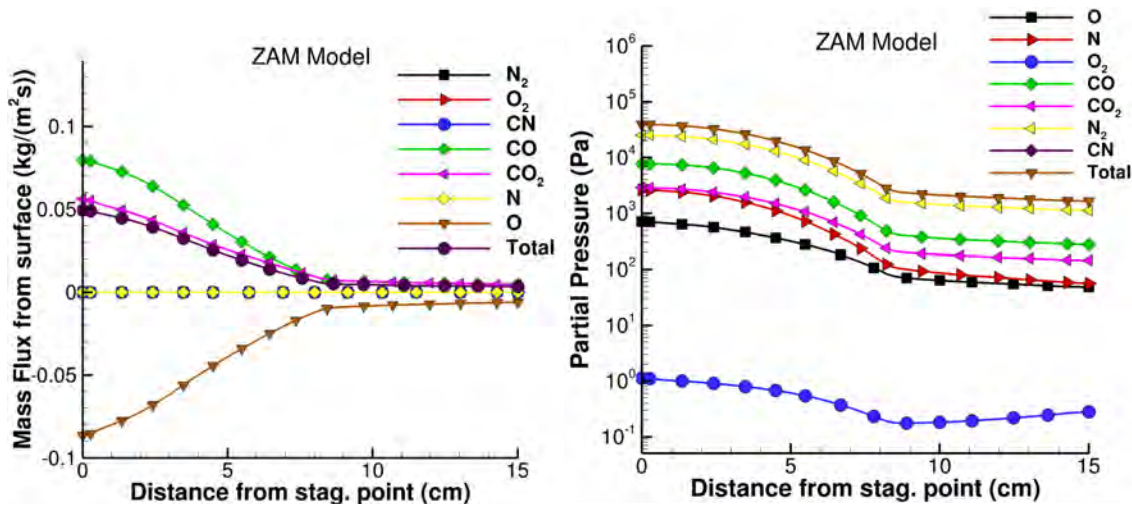


Figure 9: Modified ZA model of MacLean et al. results for (a) mass flux off the surface and (b) near-wall composition (note that CN levels are below 10⁻¹ Pa).

I.6 Ablation Model Validation with VKI Plasmatron Tests (On-Going)

We are continuing to compare our simulated results with experimental data from the von Karman Institute (VKI) for Fluid Dynamics; a research institute in Belgium that has recently received an AFOSR grant on ablation in 2018. A crucial aspect of comparing simulations with experimental data is accurate characterization of the free-stream conditions. Over many years, researchers at the VKI have developed and used a method called the Local Heat Transfer Simulation (LHTS) method. Specifically, given the complex inductively coupled plasma generation procedure, the free-stream enthalpy for each experimental run would have significant uncertainty. To reduce this uncertainty, each experiment begins by inserting a cold, highly catalytic, probe into the flow. Since the wall boundary conditions are controlled ($T=300$ K and fully catalytic), and since the flow upstream of the boundary layer (in the plasma jet) can be assumed in thermochemical equilibrium (due to subsonic flow conditions), one can use the measured cold-wall heat flux to “reconstruct” what the enthalpy upstream of the boundary layer must be. After this cold-wall heat flux is measured, the copper probe is removed from the flow and an ablative sample is introduced (while the plasma torch continues to operate). In this manner, for each experiment, the free-stream enthalpy can be more accurately determined. While the VKI LHTS method is only applicable in 1D (along the stagnation streamline), we aim to characterize the free-stream using 3D US3D simulations, and then use the same 3D CFD capability to simulate flow over the ablative samples. For example, Fig. 10 shows a US3D simulation where the cold-wall heat flux is matched between simulation and experiment.

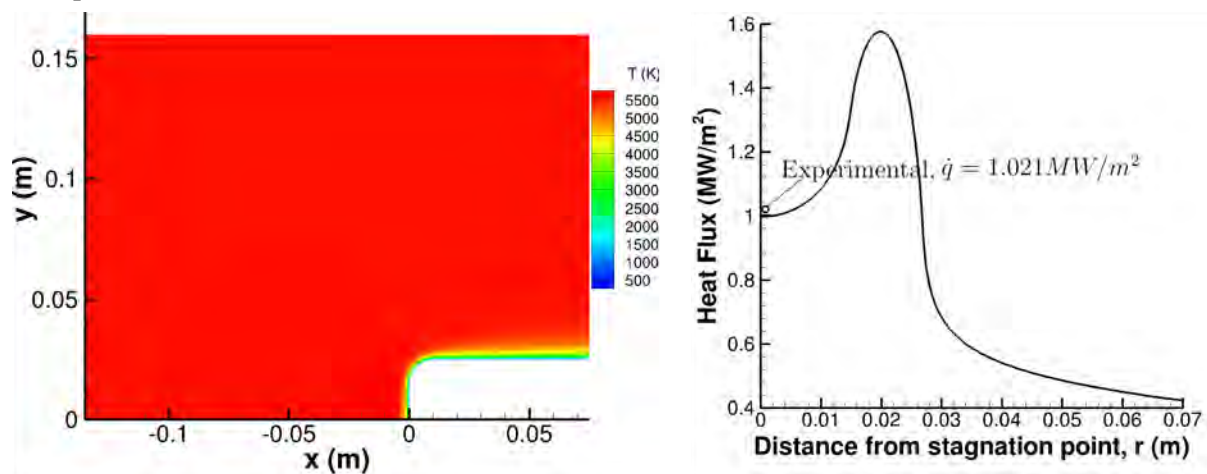


Figure 10: (a) Temperature contours for subsonic plasma flow over a TPS sample geometry matching that tested in the Plasmatron facility at the VKI [31]. (b) Computed heat flux profile around the sample surface corresponding to the cold copper probe used to calibrate the ablation experiments (wall is fixed at 300 K and is fully catalytic), compared to the experimentally measured stagnation point heat flux.

Several experimental conditions were simulated, with conditions taken from Ref. [31]:

Helber, Chazot, Hubin, and Magin, “Microstructure and gas-surface interaction studies of a low-density carbon-bonded carbon fiber composite in atmospheric entry plasmas”, *Composites Part A: Applied Science and Manufacturing* 72 (2015) pp. 96-107.

Example results are shown in Fig. 11 and Table 2. To summarize briefly, the simulations indicate that (i) US3D simulations are able to predict cold-wall heat flux in close agreement with experimental measurement (Fig. 10 and Table 2), (ii) US3D predicts the flow to be in thermal equilibrium ($T=T_v$) everywhere except for some nonequilibrium in the thin boundary layer region (Fig. 11a), thereby supporting the assumptions of the LHTS method, (iii) the boundary layer edge temperature (Fig. 11a) and enthalpy (Fig. 11b) predicted by US3D simulations are very close to those “reconstructed” by VKI researchers using the 1D LHTS method, while the velocity at the boundary layer edge (Fig. 11c) shows the most difference between US3D and LHTS. Table 2 summarizes these comparisons for three different

experimental conditions. The main point is that, while a variety of free-stream conditions could lead to the same stagnation point heat flux, there is only one way to obtain such consistent results (comparing US3D/LHTS/measurement) for the free-stream enthalpy, boundary layer edge properties, and heat flux. The results are promising, in that they provide evidence that the freestream conditions used in US3D simulations are representative of the actual free-stream in the facility, and when the simulations are performed, we can reproduce the measured cold-wall, full catalytic, heat flux.

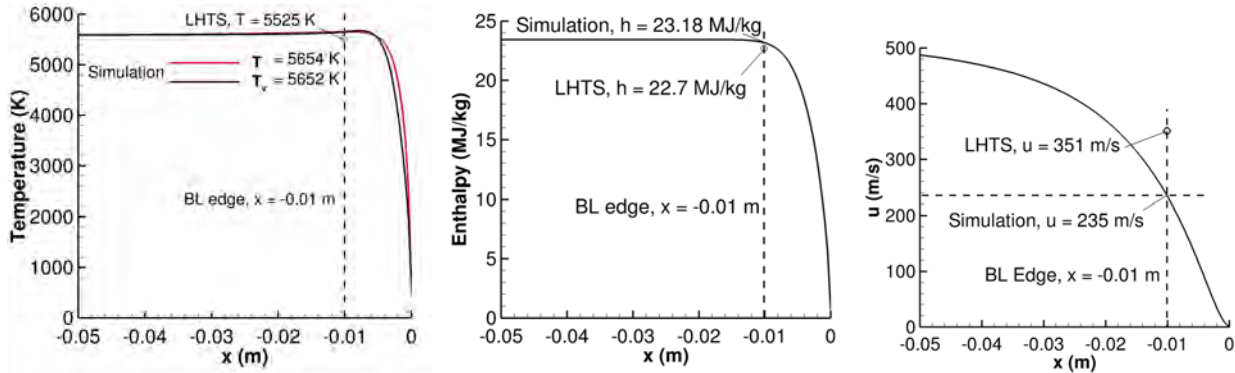


Figure 11: US3D simulation results along the stagnation streamline for Case 1 (in Table 2). (a) Temperature profiles, (b) Enthalpy profiles, (c) X-velocity profile. Note that the boundary layer edge has a strict definition used to interpret both LHTS and US3D results.

Table 2. Comparison of US3D simulation results with experimentally inferred results (using the LHTS method). Note that heat flux is measured experimentally and not inferred.

Case	u_e (m/s)	u_s (m/s)	T_e (K)	T_s (K)	$T_{v,s}$ (K)	h_e (MJ/kg)	h_s (MJ/kg)	\dot{q}_e (MW/m ²)	\dot{q}_s (MW/m ²)
1	351	235	5525	5654	5652	22.7	23.18	1.02	1.00
2	232	194	5460	5966	6009	21.4	28.2	1.02	0.95
3	232	187	5600	5887	5944	22.6	30.89	1.06	0.96

u - x-velocity h - specific enthalpy \dot{q} - heat flux e - experimental s - simulation

With an accurately characterized free-stream, as discussed above, we are now running US3D simulations with the new ablation models in order to compare with the ablation measurements taken for these experiments.

I.7 Experimental Measurements of Microstructure Influence

The overall goal of this experimental campaign, carried out by Prof. Erica Corral’s group at the University of Arizona, was to gain a fundamental understanding of the effect of microstructure on ablation responses from three different graphitic materials by correlating their ablation rates with the corresponding microstructural evolutions.

Results are analyzed for conditions in the reaction-rate limited regime, since the microstructural nature of a graphitic specimen directly determines the reactivity of the active carbon sites/atoms and hence, affects the reaction rate. For approximate analysis, the experimental data is fit by phenomenological models for all three kinetic regimes, while considering the microstructural influence, to predict ablation rates for graphitic materials with similar microstructural characteristics under designated experimental conditions. Results related to ablation of different graphitic microstructures in this report are described in Ref. [32].

Oxidation tests were performed in a thermogravimetric analyzer (TGA). The TGA furnace (Netzsch STA 449 F3 Jupiter, Selb/Bavaria, Germany), as shown in Fig. 12 (a), is used to perform ablation experiments under thermal equilibrium and controlled linear gas flow environment (laminar flow). The furnace capabilities are listed in Table 3. To properly interpret the experimental data, a commercially available

computational fluid dynamics (CFD) software (COMSOL Multiphysics, Boston, MA) has been implemented to analyze the gas flow condition inside the furnace chamber, especially within the gas boundary layer around the specimen during oxidation. Using 200 mL/min as input gas flow rate, a calculated gas velocity map showing the surrounding gas in the vicinity of the specimen is shown in Fig. 12 (b).

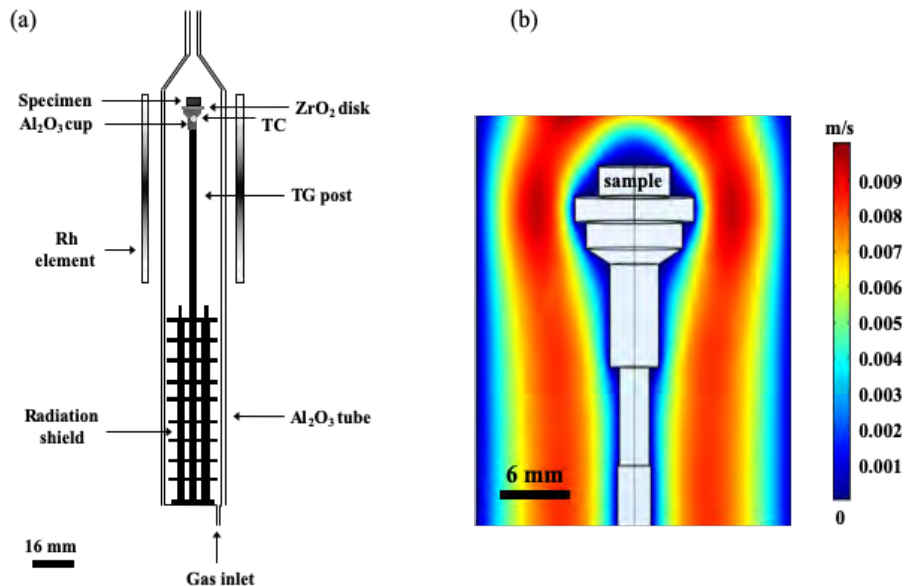


Figure 12: (a) TGA setup for oxidation testing under controlled pressure and low gas flow environment. Inside the furnace chamber a TG post that is connected to a scale at the bottom and the sample rests on a zirconia disk atop the post. (b) Gas flow velocity map around the sample generated via CFD approach using COMSOL Multiphysics © software using a gas flow of 200 mL/min.

Table 3. Typical TGA furnace capabilities

Temperature range	0 to 1600°C
Heating rate	0.001 to 50°C/min
Flow rate	2 to 260 mL/min
Maximum acquisition rate	30 points/°C or 600 points/min
Gas species	Air, oxygen, argon, nitrogen, and helium

Highly ordered pyrolytic graphite (HOPG, PG5, K&J Magnetics, Inc., Pipersville, PA), isotropic graphite (Isocarb-85 or I-85, Electrodes Inc., Milford, CT), and carbon-carbon (C-C) composite (Hitco Inc., Gardena, CA) were ablated over a wide range of oxidation test conditions in order to determine the effect of microstructure on their ablation response. The densities of isotropic graphite and HOPG are 1.85 and 2.27g/cm³, respectively. The C-C composite discs were a 2D composite comprising T300-3K fibers in an 8-harness satin weave, densified to ~1.6 g/cm³ by chemical vapor infiltration with carbon black used as the matrix material [33]. The specimens are cut and sanded to size and weighted, with HOPG and I-85 being 4 mm × 4 mm × 2 mm, and C-C being 6 mm (diameter) × 2.5 mm (height) in dimension. The weight for the specimens ranges from 0.07 to 1 g. Prior to oxidation testing, all specimens are washed ultrasonically in 1 M hydrogen chloride (HCl) for 10 minutes, followed by a one-minute wash in acetone, isopropanol, and DI water, respectively, to remove impurities. Microstructures of the three graphitic materials before oxidation are shown in Fig. 13.

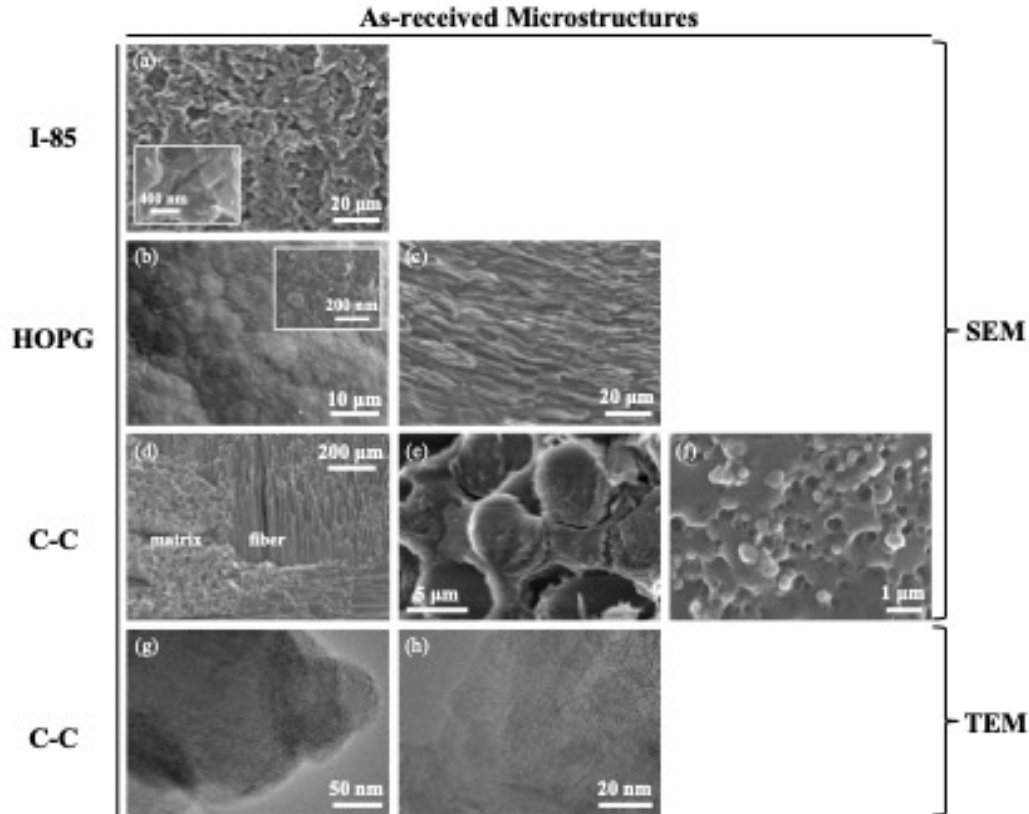


Figure 13: As-received microstructures of I-85 (a), HOPG [(b)pristine surface and (c) highly oriented graphitic sheet edges with c-axes perpendicular to the planar surface], C-C composite [(d) overview, (e) x-sectional view of carbon fibers embedded in the carbon black matrix, (f) heterogeneous structure of carbon black matrix, (g) shell-core structure of a spherical carbon black particle in the matrix, and (h) short-range order of “graphite-like” binder material in the matrix]. Micrographs (a) to (f) are acquired using SEM, and micrographs (g) and (h) are acquired using TEM.

Since the three graphitic materials possess completely different microstructures, scanning electron microscopy (SEM) (S-4800, Hitachi Inc., Chiyoda, Tokyo, Japan, and Helios NanoLab 660 DualBeam FIB/SEM, Thermo Fisher Scientific Inc., Waltham, MA) as well as transmission electron microscopy (TEM, only on selected structure) (HF5000 TEM/STEM, Chiyoda, Tokyo, Japan) are used to characterize their microstructural changes before and after isothermal oxidation in order to gain insights on their ablation mechanisms. A detailed microstructural analysis is performed primarily for specimens oxidized at 650 °C as the ablation processes of the three graphitic specimens are mostly within the reaction-rate limited regime, and the oxidation rates are relatively slow compared to those at high temperatures and allow us to capture the morphologies of these graphitic materials during the beginning or intermediate stages of oxidation. We measured the mass loss of the three graphitic materials from 650 to 1600 °C. The ablation rates are plotted in logarithm scale versus the reciprocal of the absolute temperature (to obtain linear Arrhenius rate curves in each kinetic regime) with the rates of HOPG represented in dark grey squares, I-85 in black circles, and C-C composite in light grey diamonds as shown in Fig. 14.

At moderate temperatures (650 to 800 °C), as shown in Fig. 14, I-85 and C-C exhibit similar ablation rates with I-85 ablates approximately 1.9 times faster at 650 °C and gradually reduces the factor to 1.3 as the temperature increases. However, the ablation rate of HOPG at 650 °C is approximately 390 times slower compared to the other two materials and maintains about two orders of magnitude slower at temperatures below 800 °C, which agrees with the observation made by Rosner [34]. The average activation energy (E_a^I) of HOPG within is about 172.77 kJ/mole, calculated from the slope of the

corresponding ablation rate curve. This value is in excellent agreement with the literature reported values. Levy and Wong [35] measured an average activation energy of 179.912 kJ/mole for pyrolytic graphite oxidized between 760 to 871 °C under airflow velocity of 0.25 to 1 m/s. Stevens et al. [36] conducted experiments between 500 to 800 °C under 130 Torr (~17.33 kPa) pO₂ and obtained an active energy for monolayer etching (carbon removal from the edge of a basal plane) of 168 ± 5 kJ/mole, and an active energy for multilayer etching (carbon removal from both the surface and the edge of a basal plane) of 175 ± 3 kJ/mole. A few years later, within a temperature range of 875 to 950 °C under dry air, Hahn [37] measured the activation energies for vertical (carbon removal from the surface of a basal plane) and lateral (carbon removal from the edge of a basal plane) etching of 193 and 143 kJ/mole, respectively. The values of E_a^I for I-85 and C-C composite are calculated as 62.1 kJ/mole and 83.8 kJ/mole. In contrast with HOPG, whose “available” reaction sites only come from the substrate edges and the limit amount of naturally existed surface defects, the microstructure of I-85 and C-C contains a much higher fraction of edge-carbons. Hence, it makes sense that their values of E_a^I should be close to or smaller than the activation energy reported for carbon removal from the edge of a basal plane, which should be lower in magnitude compared to E_a^I for surface-carbon removal owing to the higher electronic density.

Upon increasing temperature (900 to 1000 °C), the three graphitic materials exhibit very similar ablation rates with the rate for HOPG experiencing a sudden increase from 800 °C to 900 °C (indicated by the bold squiggly arrow) and becomes only 1.3 to 1.4 times slower than the other two materials as shown in Fig. 14. This abrupt jump in ablation rate suggests a change in the ablation mechanism in which the thermal energy is sufficient to activate carbon removal from the basal plane in the vertical direction. In this case, the abstraction of carbon atoms is no longer limited to lateral etching of the atoms from substrate edges and existed defects but also from vertical etching of the pristine basal planes, which generates new surface defects for further oxidation reactions [37][38]. Levy reported the same discontinuity in the rate curve at 843 °C from oxidizing a pyrolytic graphite specimen [31]. At higher temperatures (1200 to 1600 °C), HOPG, I-85, and C-C composite exhibit almost identical ablation rates, as shown in Fig. 14.

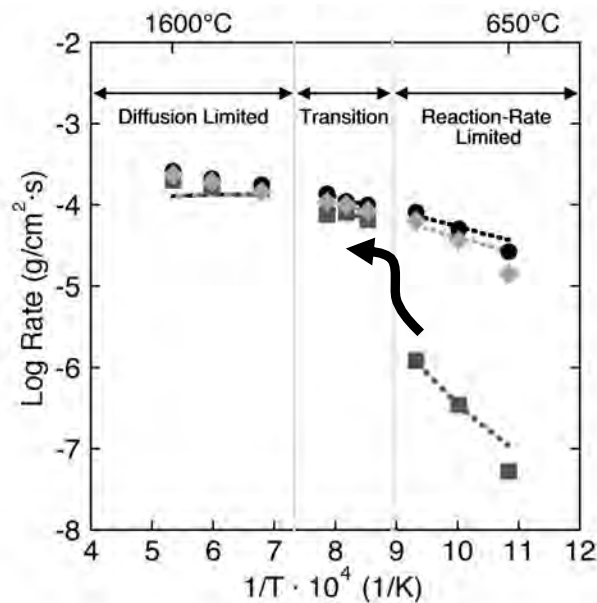
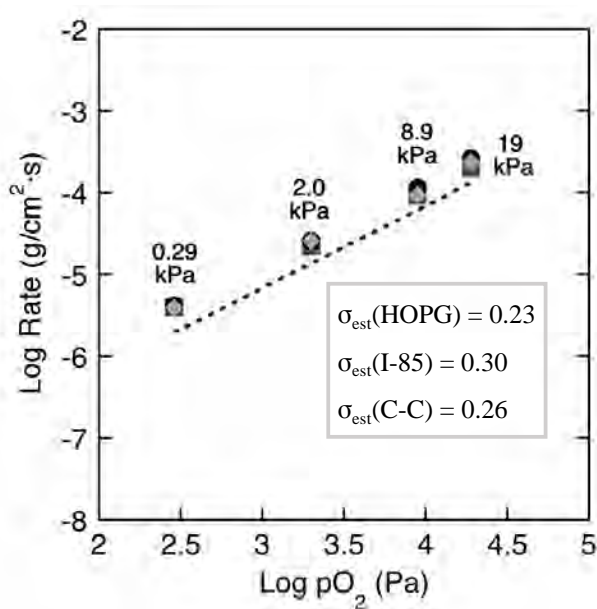


Figure 14: Experimental measured mass loss rates from 650 to 1600 °C under 19 kPa for HOPG (dark grey squares) , I-85 (black circles), and C-C (light grey diamonds). The corresponding model predicted mass loss rate for each material is represented using a dashed line of the same color as the geometry. An abrupt increase in mass loss rate of HOPG between 800 to 900 °C is indicated by a black squiggly arrow.

The ablation rate as a function of the partial pressure of oxygen (pO_2) was also measured for HOPG, I85, and C-C from 0.29 to 19 kPa and plotted in Fig. 15. Here, the ablation rates are not sensitive to microstructure, i.e., the three materials show almost identical ablation rates but increase with increasing pO_2 as more O_2 molecules are available for reaction.

Figure 15: Mass loss rates of HOPG (dark grey squares), I85 (black circles), and C-C composite (light grey diamonds) oxidized within the diffusion controlled kinetic regime at 1600 °C under pO_2 of 0.29 to 19 kPa. The model predicted results for the three materials under the same testing conditions are represented by the black dashed line with the corresponding standard error of the estimation reported on the side.



Owing to the additional dissociative chemisorption step [39][40], the ablation response from molecular oxygen measured in this campaign is considerably different from that of an atomic oxygen source [14][24][34]. Calculated from the empirical data provided by Rosner et al. [34], the activation energies of pyrolytic graphite and isotropic graphite (microstructurally comparable to HOPG and I-85) being oxidized in molecular oxygen are 7.18 and 7.43 times, respectively, of the values when atomic oxygen is used. The fact that the two proportionality factors (calculated from the two distinct graphitic microstructures) are notably close in magnitude suggests that the difference in reactivity between O_2 and O is primarily caused by the required dissociation of O_2 molecules on the surface, prior to oxidation reactions. This is precisely how O_2 carbon reactions are modeled in Reaction 16 in Table 1.

1.8 C-C Composite Experiments and Possible Model Extension

Being a composite material in which the microstructure is a combination of carbon fibers and carbon black matrix, the ablation behavior of C-C composite is governed by each of these two components in addition to its processing conditions and methods. Figure 16 (a) shows an overall view of the oxidized carbon fibers and matrix. Similar to what Jacobson and Curry [41] have observed, the matrix seems to be preferentially oxidized compared to the fibers underneath. Evidence of fiber oxidation is found in regions indicated by the white arrows, where numerous narrow curling channels tracing the cylindrical surface of the fibers are developed in the sections being exposed, instead of being covered/protected by the matrix. These channels keep growing and join with other channels in the vicinity as the material gets etched away during oxidation, eventually causing the fibers to fracture. Meanwhile, the channels are believed to grow from small pits [inside the white dashed oval in Fig. 16 (a)] that are developed on the fiber surfaces at the beginning stage of the oxidation process. This observation is supported by McKee [42], who claimed to see “lenticular voids parallel to the fiber axes” on a section of a C-C composite after being oxidized at 800 °C in air. A close-up look of these small pits on the trunks of the carbon fibers captured from a matrix shielded area is given in Fig. 16 (b). Images (c) and (d) of Fig. 16 provide the morphology of the oxidized carbon black matrix. Within the matrix itself, there is preferential oxidation of the graphite-like binder over the spherical carbon black particles. As shown in part (c), a piece of graphitic binder material (traced in red dashed line) becomes very thin due to oxidation, and not only does it have holes developed on it, but also becomes translucent and reveals the carbon black particles underneath. Similarly, in part (d), the leftover graphitic binder (pointed by the red arrow) exhibits a delicate “spiderweb-like” structure that wraps around the carbon black spheres and was fluttering under the electron beam as this SEM image was

being taken. Moreover, the oxidized carbon black particles shown in both part (c) and (d) appear to have more surface textures than its un-oxidized state.

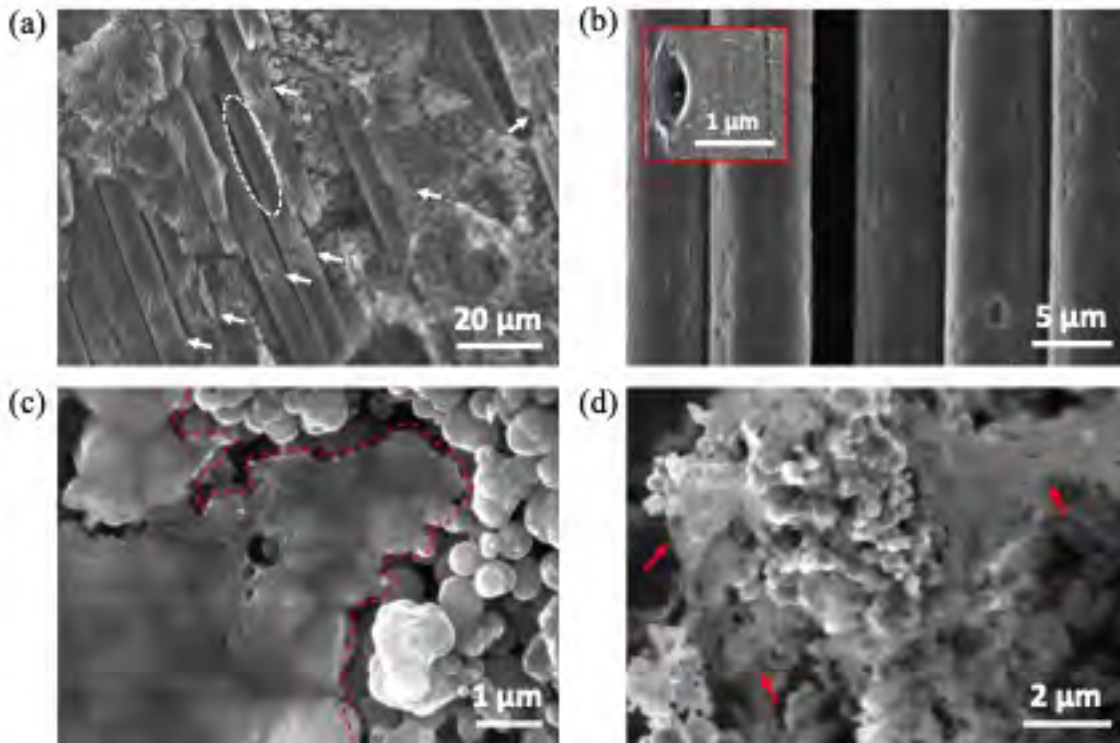


Figure 16: Microstructures of C-C composite after isothermal oxidation at 650 °C for 30 minutes under 19 kPa pO₂. (a) overall morphology of the oxidized fiber and carbon black matrix. Oxidation is believed to initiate from the small holes inside the white dashed oval, which grow into thin channels (indicated by the white arrows) before fracture occurs. (b) small holes on fiber surface with a zoom-in view show a typical elongated “leaf-like” shape given in the red box. (c) and (d) demonstrate oxidized carbon black matrix, which shows stronger oxidation resistance in the turbostratic spheres compared to the surrounding graphitic binder material.

II SILICON CARBIDE (PASSIVE-ACTIVE TRANSITION AND T-JUMP)

II.1 Background and Motivation

Silicon carbide (SiC) based composites form a surface layer of SiO₂ when exposed to oxygen [43,44]. This layer often protects the underlying SiC material from oxidation reactions that remove Si and C, and therefore this SiO₂ layer may prevent significant TPS mass loss. Similar oxide layers form on more complex UHTC materials of interest to the Air Force. However, higher surface temperatures and/or lower partial pressures of oxygen can lead to rapid removal of the SiO₂ layer. The formation of the SiO₂ layer is referred to as *passive oxidation* while the removal of the SiO₂ layer and oxidation of the underlying material (SiC for example) is referred to as *active oxidation*. In a number of high enthalpy flow experiments [43,45-52] passive to active oxidation has been studied, and in a number of cases, sudden increases in TPS surface temperature have been observed even when free-stream flow conditions were held constant. This phenomenon is commonly referred to as “temperature jump”. For example, C/SiC TPS have been studied in Refs. [43,45-49] and Ultra High-Temperature Ceramic (UHTC) materials have been studied in Refs. [50-52]. Many similarities in high-temperature behavior are found for both SiC-based and more complex UHTC materials.

The article by Panerai et al. [43] contains a wealth of experimental data and analysis regarding the temperature jump phenomenon on C/SiC composites tested within a high enthalpy inductively coupled plasma (ICP) wind tunnel facility operated at the von Karman Institute (VKI) for Fluid Dynamics. As a particular example, Fig. 8 of Ref. [43] shows sudden surface temperature jumps from approximately 2100 K to almost 2500 K, despite the free-stream plasma flow conditions remaining constant. Further analysis in the article discusses how after such events the TPS is significantly degraded and could no longer be considered reusable [43]. The temperature jump phenomenon may be related to the transition between passive and active oxidation, however, this is not entirely clear. For example, the study in Ref. [43] observed that the jump occurs within the active oxidation regime (beyond the passive to active oxidation transition). In this project, a series of molecular beam experiments are performed on SiC in order to study the active-passive transition and investigate possible explanations for the temperature-jump delay.

II.2 Molecular Beam Experiments on SiC with Thin Oxide Layer

We have conducted new molecular beam experiments on the oxidation of SiC, with the goal of understanding the details of both the transition from passive to active oxidation and the temperature jump. Fig. 17 summarizes the first set of experiments, which focused on the decomposition of a thin oxide layer on SiC. We started with 6H-SiC samples and exposed them to a high fluence of atomic oxygen in a hyperthermal atomic-oxygen beam produced by a laser-detonation source. This exposure created a silicon dioxide layer on the surface that is estimated to be ~5 nm thick. XPS analysis verified the formation of an SiO₂ layer. Then we placed oxidized samples in a heated sample mount in a vacuum chamber (base pressure ~ 10⁻⁷ Torr) in front of a mass spectrometer for further experimentation. We first heated a sample without any further O-atom exposure and monitored the mass spectrum of products that evolved from the surface as the sample temperature was increased. A sudden spike in the signal at a mass-to-charge ratio, m/z , of 44 was observed at a temperature of 1670 K, and then this signal disappeared quickly as the temperature was increased further. Because the signals at $m/z = 44, 45,$ and 46 were consistent with the natural isotopic abundances of ²⁸Si, ²⁹Si, and ³⁰Si, we assigned the product detected at $m/z = 44$ as SiO. Thus, when the oxidized sample is heated in vacuum with no O-atom exposure, the oxide layer apparently decomposes to SiO gas at a temperature of ~1670 K.

In a second study, we placed a sample that had been pre-oxidized in the same manner as described above in the heated sample mount and conducted a molecular beam-surface scattering experiment. The experimental set-up was the same as that shown on the right side of Fig. 17. For this experiment, a pulsed hyperthermal beam containing 93% O and 7% O₂, with an average velocity of 7770 m s⁻¹, was used without velocity selection with a chopper wheel.

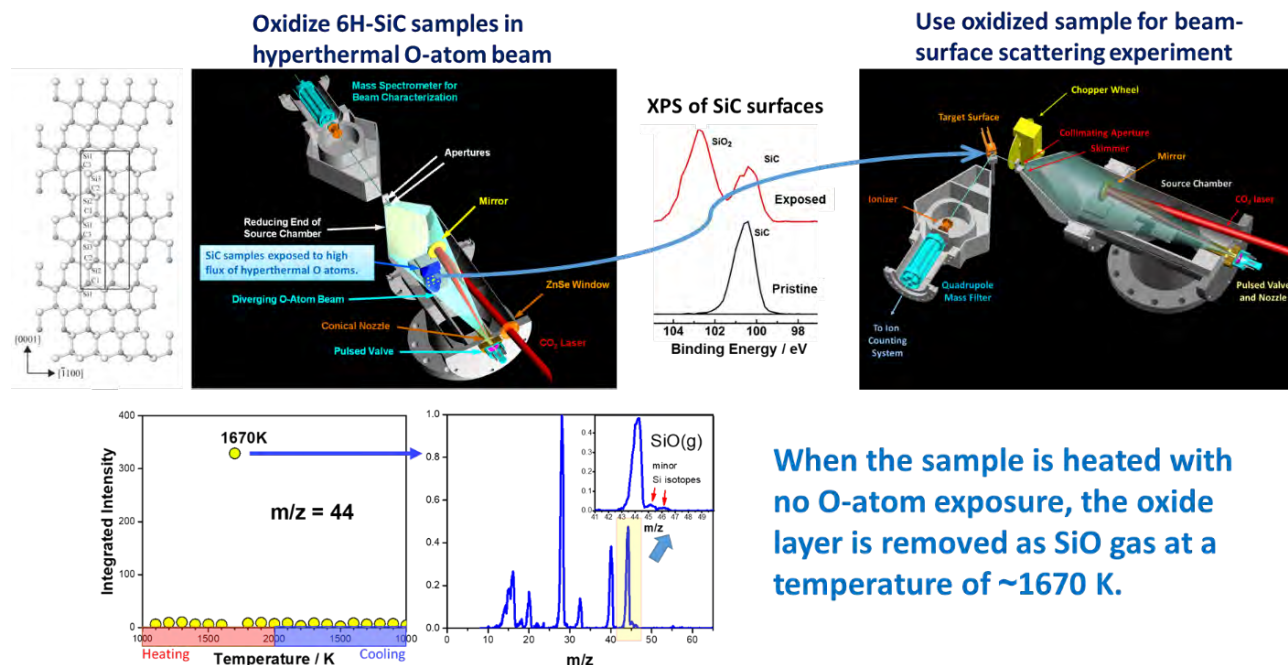


Figure 17: Pictorial summary of first experiment that probed the decomposition of a thin (~5 nm thick) oxide layer on 6H-SiC by mass spectrometry.

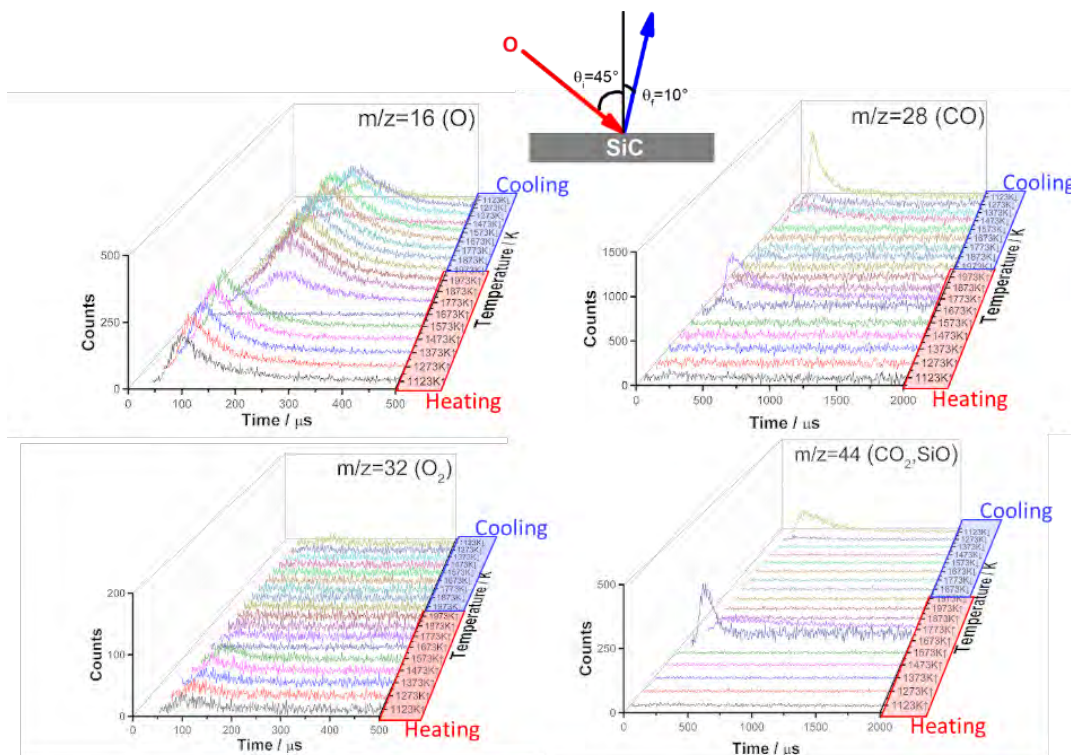


Figure 18: Time-of-flight distributions of scattered products collected at $m/z = 16, 32, 28,$ and 44 at a final angle of $\theta_f = 10^\circ$, following bombardment of a 6H-SiC surface by a pulsed hyperthermal beam containing O and O₂, with an incident angle of $\theta_i = 45^\circ$. The sample was brought to 1123 K and then heated in (mostly) 100 K steps to 1973 K and then cooled back to 1123 K in (mostly) 100 K steps.

While this beam was impinging on the surface at an incident angle of $\theta_i = 45^\circ$, time-of-flight distributions were collected at $m/z = 16, 32, 28,$ and 44 as a function of surface temperature at a final angle of $\theta_f = 10^\circ$. A low final angle of 10° was chosen because products that desorbed from the surface in thermal equilibrium were expected to give the highest signal along the surface normal. During data collection, the sample was heated from 1123 K to 1973 K in (mostly) 100 K increments and then the temperature was reduced in (mostly) 100 K increments until the sample temperature reached its initial value. The results are summarized in Fig. 18. Below the passive/active transition temperature, incident O atoms scatter directly – there is no evidence for thermal accommodation of O on the SiO_2 surface. When the sample rises above the passive/active transition, there is an abrupt change in the scattering dynamics of O, as the O that exits the surface desorbs in thermal equilibrium with the surface. The thermal desorption of O atoms is very similar to the results that we have observed previously in analogous molecular beam-surface scattering experiments on vitreous carbon. O_2 , which is present in the incident beam, appeared to scatter directly at lower temperatures, and then the signal became very weak and made the scattering dynamics very difficult to discern at temperatures above the passive/active transition. The reduction in the O_2 signal at $\theta_f = 10^\circ$ is likely the result of a change in the angular distribution of the O_2 products, which shifted to larger angles because the surface became covered with a smooth graphitic layer (see below). At lower temperatures and near the transition temperature, CO and CO_2 may be formed in mainly thermal processes (the signals are difficult to see on the scale of the graphs in Figure 18). When the sample approaches the passive/active transition temperature, it appears that there is a sudden increase in the evolution of products that are detected at $m/z = 28$ and 44 . We believe the $m/z = 28$ signal to arise from CO and the $m/z = 44$ signal to arise from SiO. Both signals drop dramatically as the temperature is incremented further. Assuming the assignment of the signals is correct, then it seems that as the passive/active transition is approached, CO and SiO reaction products thermally desorb from the surface at relatively high fluxes and then these signals decline quickly as the temperature increases further. The underlying mechanisms that lead to the observed signals are not currently understood and require more study. The lack of reactive signals ($m/z = 28$ and 44) at temperatures well above the passive/active transition temperature indicates surface passivation. When the surface temperature is reduced, reactive signals at $m/z = 28$ and 44 appear, and the O signal has the dynamical character that is representative of thermal desorption, which is qualitatively different than the O signals that were observed originally from the oxidized SiC surface.

Clearly, the oxidized SiC surface underwent a transformation when it was heated and then cooled. Based on the scattering data and general knowledge that a graphene-like layer can be formed by heating SiC, we speculated that a graphitic layer was formed on the surface at temperatures above the passive/active transition, where the SiO_2 layer presumably was removed. If this is the case, then we would assign the $m/z = 28$ and 44 signals from the surface that had been cooled back to 1123 K to come from CO and CO_2 , respectively. The observations of significant CO and CO_2 signals and thermal desorption of O atoms at relatively low temperatures are consistent

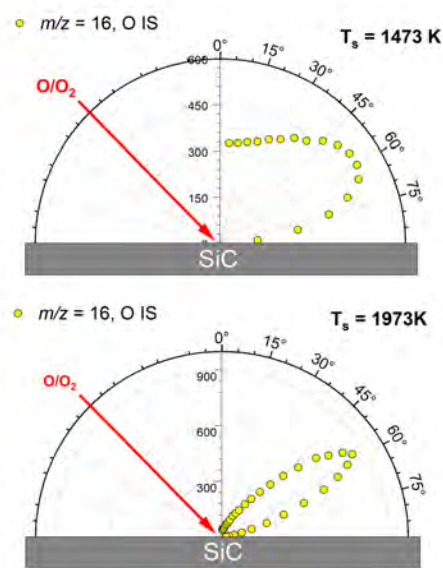


Figure 19: Angular distributions of scattered O-atom flux from an oxidized 6H-SiC surface at a lower temperature and the same surface after it had been heated to a higher temperature. During heating the surface was bombarded at $\theta_i = 45^\circ$ by the pulsed hyperthermal beam containing O and O_2 , and time-of-flight distributions were collected at a variety of final angles at $m/z = 16$. The relative flux was derived by appropriate integration of each time-of-flight distribution.

with our observations from our earlier molecular beam studies of the oxidation of vitreous carbon and graphite. As discussed below, additional studies added weight to this supposition.

Figure 19 shows angular distributions of scattered O-atom flux from the oxidized SiC surface at a lower temperature and the SiC surface at a higher temperature that had presumably lost its SiO₂ layer and become covered with a graphitic layer. At the lower temperature, which is below the passive/active transition temperature, O scatters in a broad angular distribution, indicative of scattering on a surface that is rough on an atomic scale. Above the transition temperature, O scatters in a narrow angular distribution, indicative of scattering on an atomically smooth surface. Such scattering dynamics are consistent with a smooth graphene-like surface.

XPS analysis of the surfaces on SiC that resulted from different treatments was performed and compared to XPS analysis of a pristine 6H-SiC surface (Fig. 20). These results are consistent with the formation of a graphitic layer on the surface after the oxidized SiC sample was heated to a temperature above the passive/active transition. Finally, the presence of a graphitic layer was also confirmed by a Raman scattering analysis of the surface that had been heated to 1973 K (not shown).

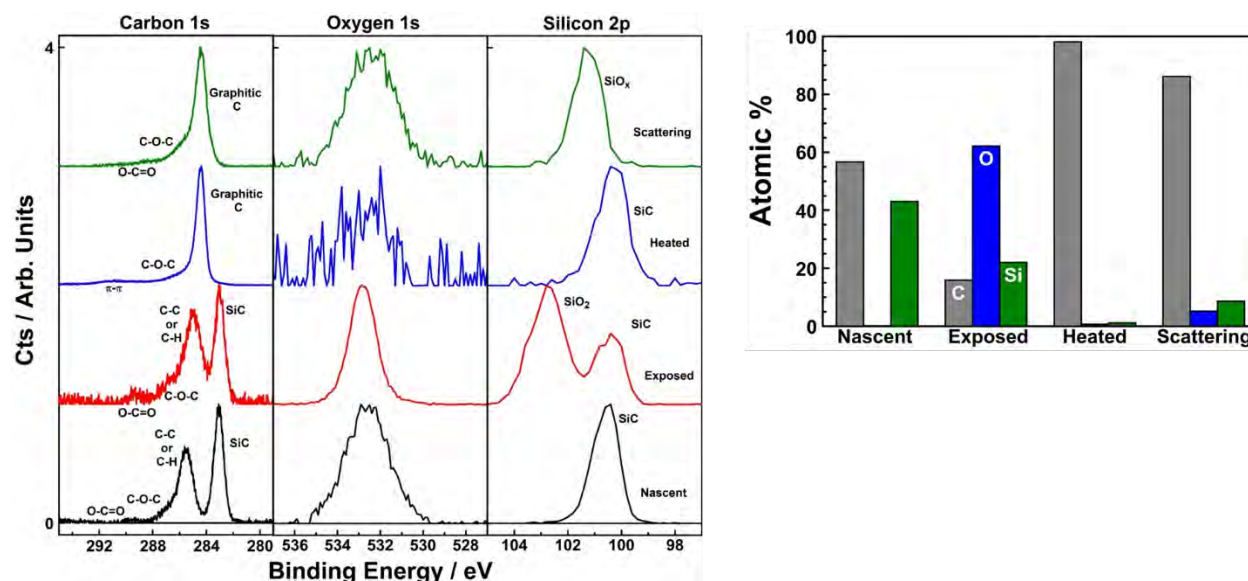


Figure 20: XPS results from a pristine SiC surface (Nascent), an SiC that was oxidized in the hyperthermal O/O₂ beam, 40 cm from the source, at room temperature (Exposed), an SiC surface that had been first oxidized and then heated to a temperature of 1973 K in vacuum (Heated), and an SiC surface that had been first oxidized and then heated to a temperature of 1973 K and then cooled to 1123 K, during bombardment by the O/O₂ beam at a distance of 99 cm from the source (Scattering). The “Scattering” sample was used during the collection of the data shown in Figs. 17 and 18.

Thus, all the results together suggest a picture where SiO is released from an oxidized SiC surface in a passive-to-active transition at about 1670 K and leaves a graphitic carbon layer that is not etched away by the relatively low flux of O atoms from the beam. If the flux of O atoms were higher, as in a real hypersonic flow (or a plasma torch facility), then the graphitic layer would presumably react more quickly to form CO, and it would not be passivating. With the removal of the passivating graphitic layer on a SiC surface that is above the passive/active transition temperature, incident O atoms could then react with SiC to form volatile SiO and CO. This active oxidation regime would result in etching of the SiC, and it could possibly result in a temperature jump because the reactions are exothermic and would release heat to the surface. Given our data on the formation of a passivating graphitic layer, one might speculate that the delay in the temperature jump after the passive/active transition temperature has been reached might

be the result of a passivating graphitic layer that needs to be removed before the full suite of high-temperature oxidation reactions can take place.

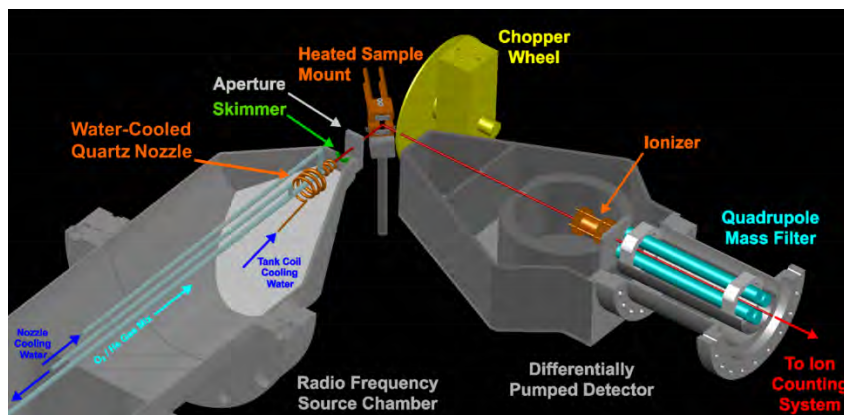


Figure 21: Schematic diagram of the experimental setup for beam-surface scattering experiments, depicting the radio frequency molecular beam source, heated sample, mechanical chopper wheel, and rotatable mass spectrometer. The key components of the mass spectrometer are the electron-impact ionizer (electron energy of 55 eV), quadrupole mass filter, and Daly-type ion detector (not shown). Ion deflector plates to prevent residual ions in the incident beam from striking the sample and a water-cooled copper surface to protect the chopper wheel from radiative heating from the hot sample are not shown.

In order to break through the passivating graphitic layer and probe the volatile oxidation products of SiC during active oxidation, we conducted a molecular beam-surface scattering experiment with a continuous beam that had a 2-3 orders-of-magnitude higher O-atom flux than the pulsed hyperthermal beam used for the experiments described above (see Fig. 17). A schematic diagram of the new experimental setup is shown in Fig. 21. This figure shows a molecular beam-scattering apparatus that is fitted with a high-pressure radio frequency (RF) discharge source for producing a continuous supersonic beam containing O atoms with velocities of $\sim 2000 \text{ m s}^{-1}$. The continuous beam was directed at a heated 6H-SiC surface, and the products that scattered from the surface were detected with a rotatable mass spectrometer. In this configuration, a mechanical chopper wheel was placed in front of the detector to modulate the products that scattered continuously, in steady state, from the surface. Time-of-flight distributions, $N(t)$, of short pulses of products that passed through slots on the chopper wheel at a given angular position of the mass spectrometer were accumulated as a function of flight time from the chopper wheel to the ionizer of the mass spectrometer. The total relative flux of a particular product corresponding to a specific set of incident and final angles was obtained by appropriate integration of the relevant TOF distribution. O_2 gas was used as the precursor for the production of a beam containing O and O_2 , with a mole ratio near 1:1. The flux of O atoms onto the sample surface was estimated to be $4 \times 10^{16} \text{ atoms cm}^{-2} \text{ s}^{-1}$. This flux was sufficient to cause significant etching of the SiC sample during the experiment, as may be seen in the photos in Fig. 22, which show the sample before and after it was exposed to the O-atom beam.

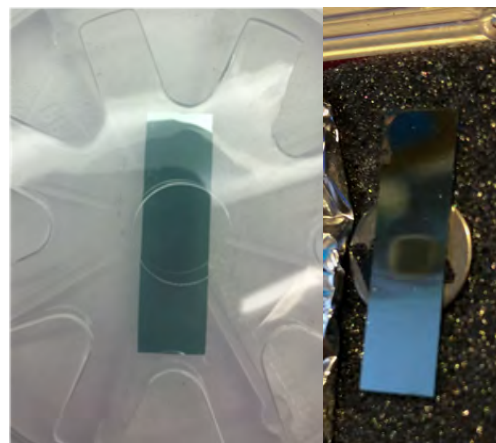


Figure 22: Silicon carbide wafer before (left) and after (right) heating and bombardment by continuous atomic oxygen beam.

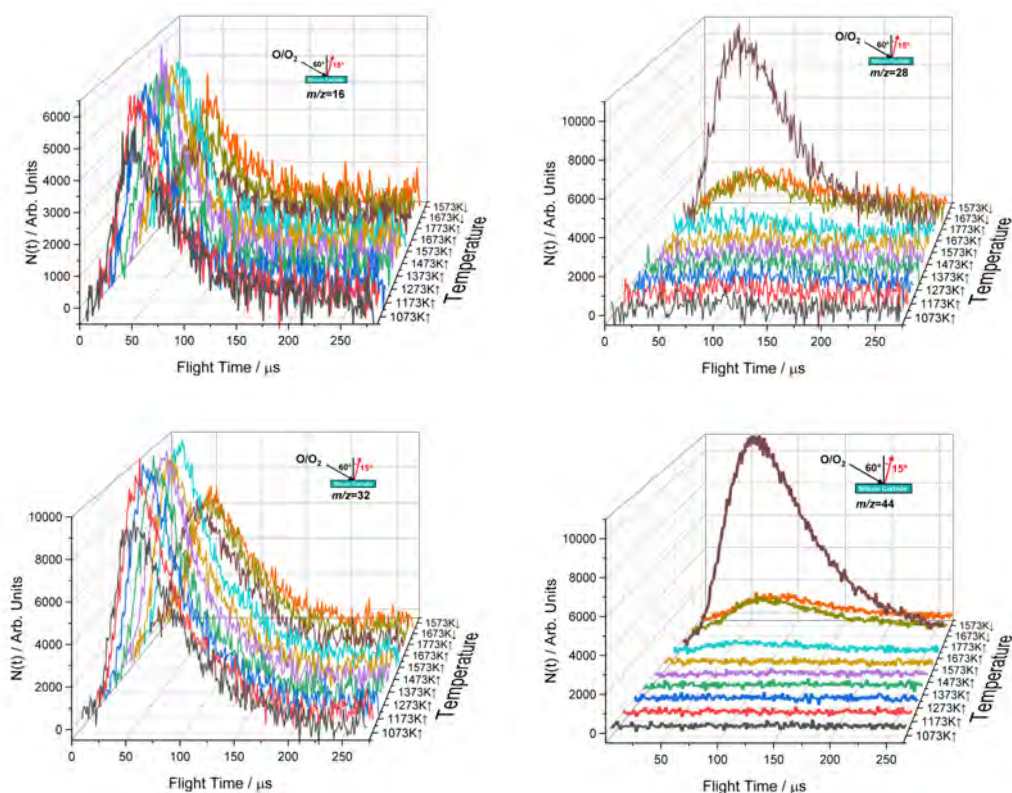


Figure 23: Time-of-flight distributions of scattered products collected at $m/z = 16, 32, 28,$ and 44 at a final angle of $\theta_f = 15^\circ$, following bombardment of a 6H-SiC surface by a pulsed hyperthermal beam containing O and O₂, with an incident angle of $\theta_i = 45^\circ$. The sample was brought to 1073 K and then heated in 100 K steps to 1773 K and then cooled back to 1573 K in 100 K steps, after which data collection stopped and the sample was cooled to room temperature and removed from the chamber.

The time-of-flight distributions for the four m/z ratios where signal was observed with continuous O-atom bombardment of the 6H-SiC surface are shown in Fig. 23. The signal at $m/z = 16$ comes from the thermal desorption of O atoms that underwent no net reaction on the surface. The time-of-flight distributions remain unchanged with increasing surface temperature until 1773 K, when the signal suddenly drops, probably because the reactivity of the incident O atoms increases abruptly. The signal at $m/z = 32$ arises mostly from non-reactive scattering of O₂ molecules that are in the incident beam. These molecules apparently come into thermal equilibrium with the surface before desorbing. It is also possible that some fraction of the O₂ signal comes from O-atom recombination on the surface. The O₂ time-of-flight distributions also remain essentially unchanged with surface temperature until a temperature of 1773 K is reached, at which point the O₂ signal suddenly drops. Either O₂ can react with the SiC surface at this high temperature or the changes in the surface at this temperature reduce the likelihood of O-atom recombination. There is very little signal detected at $m/z = 28$ at lower surface temperatures, and then the signal at this m/z ratio increases dramatically when the surface temperature reaches 1773 K. This observation is consistent with a process where the surface is covered with a passivating oxide layer at lower temperatures, resulting from bombardment by oxygen atoms, and then the oxide layer decomposes at a high temperature and allows the O atoms to react with the SiC to produce CO. This explanation assumes that a passive-to-active transition occurs at a temperature that is slightly lower than 1773 K. Given that the experiments with the pre-oxidized surface described above exhibited a clear passive/active transition at ~ 1670 K, the somewhat higher temperature of the passive/active transition during exposure to the continuous O-atom beam suggests that the higher O-atom flux of this beam delays the onset of the

transition. The signal at $m/z = 44$ also dramatically increases above the passive/active transition to a temperature of ~ 1773 K. This signal is the result of O-atom reactions to form SiO. Thus, it appears that at high temperatures where a passivating oxide has decomposed, active oxidation of SiC by atomic oxygen leads to continuous production of CO and SiO, which would etch the surface.

II.3 Molecular Beam Experiments on SiC with Thicker Oxide Layer

In order to explore the passive-to-active transition region in more detail, our collaborator, John Perepezko (University of Wisconsin) prepared a 6H-SiC sample on which a SiO₂ layer had been grown. The thickness of the SiO₂ layer was 100 nm. The sample was placed in front of the mass spectrometer, as shown in Fig. 17 (right side), and mass spectra were collected rapidly as the sample was heated in vacuum from about 1300 K to 1873 K. During collection of the mass spectra, the sample was heated at a constant rate over a time of 600 s. The mass spectra of the volatile products as a function of temperature are shown in Fig. 24.

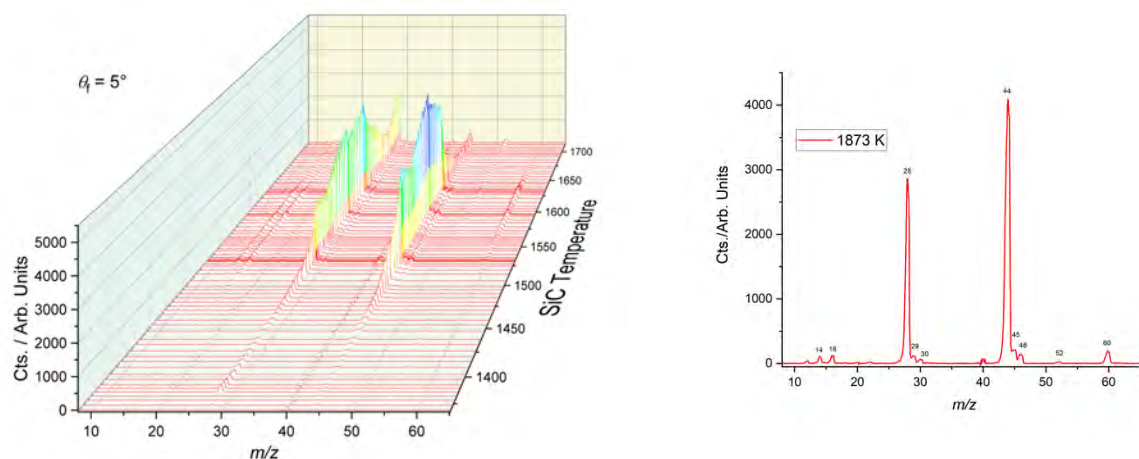


Figure 24: Mass spectra of 6H-SiC sample with 100 nm coating of SiO₂ as a function of temperature (in vacuum, no atomic-oxygen exposure). A representative mass spectrum collected at the highest temperature is shown on the right. The relative isotopic abundances for $m/z = 28, 29,$ and 30 are indicative of Si atoms, and those for $m/z = 44, 45,$ and 46 indicate SiO.

The mass spectra are dominated by two peaks at $m/z = 28$ and 44 . The relative isotopic abundances in the vicinities of these peaks suggest that they come from Si atoms ($m/z = 28$) and SiO ($m/z = 44$). It is possible that a fraction of the $m/z = 28$ signal comes from dissociative ionization of SiO in the electron-impact ionizer of the mass spectrometer, but we expect this fraction to be small, based on the fragmentation pattern of the structurally similar CO molecule. It is also possible that a small fraction of the signal at $m/z = 28$ could come from CO, but the isotopic abundances of the peaks at $m/z = 28, 29,$ and 30 strongly suggest that the product with a nominal m/z of 28 must come predominantly from a Si-containing product, which we believe to be mostly Si atoms. There is very little ambiguity in the signal at $m/z = 44$, which must come entirely from SiO. A small signal was observed at $m/z = 60$, which indicates that volatile SiO₂ is formed with low yield during the thermal decomposition of SiO₂-coated SiC. The significant thickness oxide coating on the SiC apparently results in a much slower decomposition of the oxide layer compared to what was observed for the thin oxide (Figs. 17 and 18). The relative magnitudes of the Si and SiO signals as a function of temperature are curious, but their interpretation is not possible with the current set of data. The presence of Si and SiO without significant liberation of O or O₂ is very interesting and suggests a mechanism where Si atoms from SiC are available for reaction and they react with SiO₂ to form SiO. The observation of a graphitic layer in the earlier studies of the thin oxide imply that Si atoms can be depleted from the subsurface SiC during the thermal decomposition of an oxide coating, so the results for the thermal decomposition of the thin and thick oxide coatings are consistent.

Although more work would need to be done to understand the details of the passive-active transition, including studies of the transition during O-atom bombardment, we speculate that the thermal decomposition of a thick oxide coating would significantly deplete the near-surface SiC of Si atoms and result in a relatively thick graphitic layer. The limited reactivity of graphite to oxygen at high temperatures may temporarily protect the SiC bulk from fully active oxidation until the graphitic layer has been removed. The abrupt removal by atomic oxygen of a partially passivating graphitic layer at temperatures above the passive/active transition would expose the highly reactive SiC bulk to rapid exothermic oxidation to CO and SiO; a possible explanation for the temperature jump.

III Mo-Si-B BASED COATINGS AND TESTING

III.1 Background and Motivation

UW-Madison has been focused on the examination of a new class of alloys in the Mo-Si-B system. We have also provided samples of SiC with the MoSiB based coating to Professor Erica Corral for testing and prepared single crystal SiC samples with specified oxide thickness for Professor Timothy Minton as described above. This summary highlights our work on Mo-Si-B alloys [53-58].

The phase equilibria of Mo-Si-B alloy was first studied by Nowotny [59,60] et al. in 1954. The detailed isothermal phase diagram was optimized by Perepezko [61-66] and Chang [67-70]. In the Mo-Si-B system, nearly all prior studies have focused on the Mo-rich corner, especially the $\text{Mo}_{\text{ss}}+\text{T}_2+\text{Mo}_3\text{Si}$ three phase region [71,72]. The Mo_{ss} in this three phase region has about 2.1 at.% Si (1600 °C) and 2.6 at.% Si (1800 °C) [73]. Some previous work has reported on a few compositions in $\text{Mo}_{\text{ss}}+\text{T}_2+\text{Mo}_2\text{B}$ three phase region [74,75], but this three-phase region has not been systematically studied yet.

III.2 Summary of Mo-Si-B Based Alloy Experimental Campaigns

The main research focus at the University of Wisconsin-Madison has been to pursue fundamental studies of alloy phase stability in order to design Mo-Si-B based alloys with improved mechanical properties along with maintaining good oxidation resistance. Based upon the phase stability study and our collaboration with Computherm Co. we have identified a new alloy series that fulfills the objectives. In order to provide a summary of the research developments during the project duration the main findings are briefly summarized below and a full report of UW-Madison research on the current project is attached as an Appendix.

Year One: Mo-Si-B alloys have received significant attention over the last two decades due to their high melting temperatures, creep resistance and oxidative stability, which make them exciting candidates for ultrahigh temperature applications. Phase assemblies within the Mo-MoSiB₂-Mo₃Si region are of interest for combining high strength and creep resistance and can be coated for oxidation resistance. The Mo based solid solution, with a body-centered structure, offers good toughness at elevated temperatures, but limited toughness at low temperature; the Mo₅SiB₂ phase has excellent oxidation resistance and high temperature creep resistance; the brittle Mo₃Si compound between Mo and Mo₅Si₃B also limits the mechanical performance. Thus, the existence of brittle Mo₃Si which needs to be de-stabilized. In addition, the limited ductility of the Mo solid solution has been suggested to be linked to Si solubility and/or to the effect of interstitial segregation to grain boundaries, but the understanding of these possible effects is not clear. One approach is to use computational modeling to understand the effect of multicomponent alloying on the structural stability of the T₂ and Mo₃Si phases and the influence of Si and interstitials on grain boundary cohesion.

Since Si is a known solid solution hardener in Moss, it is believed that due to Si in the α -Mo phase, the Mo-Si-B system suffers from extreme work hardening and loss of ductility at room temperature. Thus, an effort to lower the Si content in Moss can be the key to improve the ductility in Mo-Si-B alloys. In order to achieve a reduced Si content in the Moss phase we have examined the Moss+T₂+Mo₂B three phase

region. In this area, the Si solid solubility limits are 1.38 at.% (1600 oC) and 1.75 at.% Si (1800 oC) which are much lower than in the Moss+T2+Mo3Si three phase region. For the Moss+T2+Mo2B three phase region, there are still some areas that need to be clarified such as very poor oxidation resistance of Mo2B, and solution behavior of B in Moss.

In the present work, a series of Mo-Si-B alloys in the rarely studied Moss+T2+Mo2B three phase region were examined. The Moss in this three phase region has a lower Si solid solubility limit and may have better fracture toughness than alloys in the Moss+T2+Mo3Si region. The XRD results show an unusual lattice constant expansion for Moss that is consistent with interstitial solution behavior. To confirm this pm-precision analysis of STEM images was carried out to determine the solid solution type of B atom in Moss and quantitative analysis of a no-rigid registration image shows the B atom is the tetrahedral site interstitial defect. This conclusion fits the expansion of lattice constant and tiny solid solute limit of B in Moss.

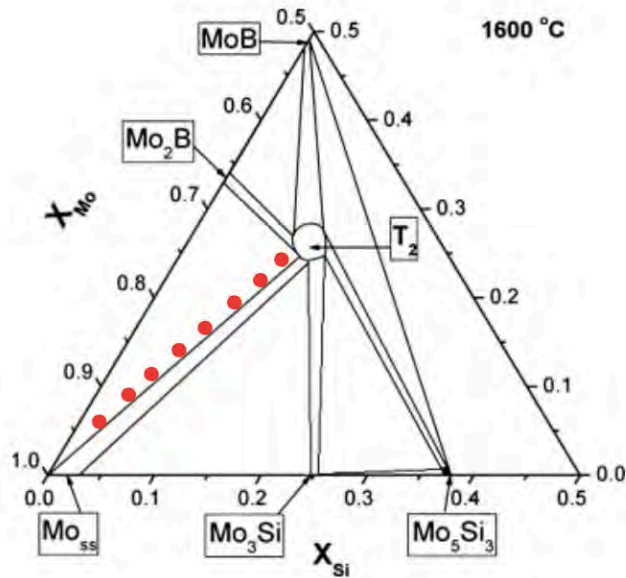


Figure 25: Mo-Si-B isothermal section for Mo-rich composition at 1600 °C. The red filled circles identify the examined alloy compositions.

Year Two: During the second period of research, the effort at UW-Madison focused on the examination of a new class of alloys in the Mo-Si-B system. We also provided samples of SiC with the MoSiB based coating to Professor Erica Corral, University of Arizona for torch exposure testing.

In this study, a series of Mo-Si-B samples in Moss+T2+Mo2B three phase region were designed to limit the content of the Mo2B phase (Fig. 25). Also, an alloy in the middle of this three-phase region was made to determine the composition of each phase by EPMA. The microstructures of the Mo-Si-B alloys in Moss+T2+Mo2B three phase region, the preliminary results on the oxidation response and microhardness- based fracture toughness are available in the full report (refer to the Appendix). In the present work, a series of Mo-Si-B alloys were designed in the Moss+T2+Mo2B three phase region. The XRD results show an unusual lattice constant expansion for Moss. The Vickers hardness tests show that the samples in Moss+Mo2B+T2 three phase region have a higher fracture toughness than the samples in Moss+Mo3Si+T2 three phase region, because the Moss in this three-phase region contains less Si. TGA result show the samples with higher T2 phase fraction have better oxidation resistance. The EPMA result shows the quantitative composition of T2 phase in this three-phase region. Mo-Si-B alloys in this three-phase region could achieve better comprehensive mechanical properties but further research is necessary.

Year Three: In the final project year, we continued our focus on the new alloy design in order to conduct a more complete evaluation of the oxidation performance over a wide temperature range. Based on initial findings on the oxidation performance, the results do confirm the benefits of low amounts of Al additions to improving both the isothermal and cyclic oxidation performance. Full details can be found in the detailed report (refer to the Appendix) and a paper is being prepared for publication.

NOTE: A full report of UW-Madison research on the current project is attached as an Appendix.

III.3 Mo-Si-B Based Coating on SiC – Torch Facility Testing

Silicon Carbide squares were slurry coated with a mixture of nitrocellulose lacquer and very fine molybdenum powder. This slurry was sprayed onto the samples with a commercial air brush. These samples were subsequently sintered at 1300°C to create a continuous layer of molybdenum powder on top of the silicon carbide samples. This process was repeated three times to build up the molybdenum layer. The samples were then coated in a pack cementation process consisting of Silicon and Boron in a 35:1 Ratio with a sodium fluoride activator and an inert alumina filler. Following the pack cementation process, the samples were conditioned in air at 1300°C for 5 hours to grow the amorphous layer.

Prepared samples were subsequently torch tested qualitatively at UW-Madison prior to shipment to the University of Arizona. Samples were placed directly into the flame of an Oxy-Methane torch set on high for times of 2 to 5 minutes. Samples accumulated torch time of upwards of 10 minutes. Mass loss measurements were only taken on samples that did not adhere to the support structure during the test. Mass losses reported from these initial torch tests ranged from 4 milligrams to 8 milligrams. Post-test examination showed a smooth and slightly porous structure present on the surface. The test results on the weight changes following the University of Arizona testing are shown below along with representative micrographs of the sample surface. Overall the weight changes are minimal indicating good performance of the coating.

Ideally, the performance of the coated samples could be compared to that of un-coated SiC samples and other UHTC samples tested in the Oxy-Methane torch at the University of Arizona. However, such direct comparisons are currently not possible as the gas-surface chemistry, unique to each type of sample, significantly effects the near-wall conditions experienced by each sample. Therefore, the conditions experienced by each sample are substantially different, given the same torch conditions. In an effort to make such material test comparisons more quantitative, the torch flow conditions must be better characterized. As part of this project, Arizona researchers have used optical diagnostics in an attempt to characterize the torch conditions, and these results are presented in the next section.

A qualitative analysis of the tests, has been performed, and is now summarized.

Exposure Conditions – Provide from the University of Arizona:

Heat Flux – 525 W/cm²

Face Temperature – 1850°C

Duration – 30 Seconds

Sample Dimensions – 0.635cm x 0.635cm x 0.381cm

Sample 1 – Retained by University of Arizona

Sample 2 Mass Loss – 0.0 mg / cm² (exposure area and total area)

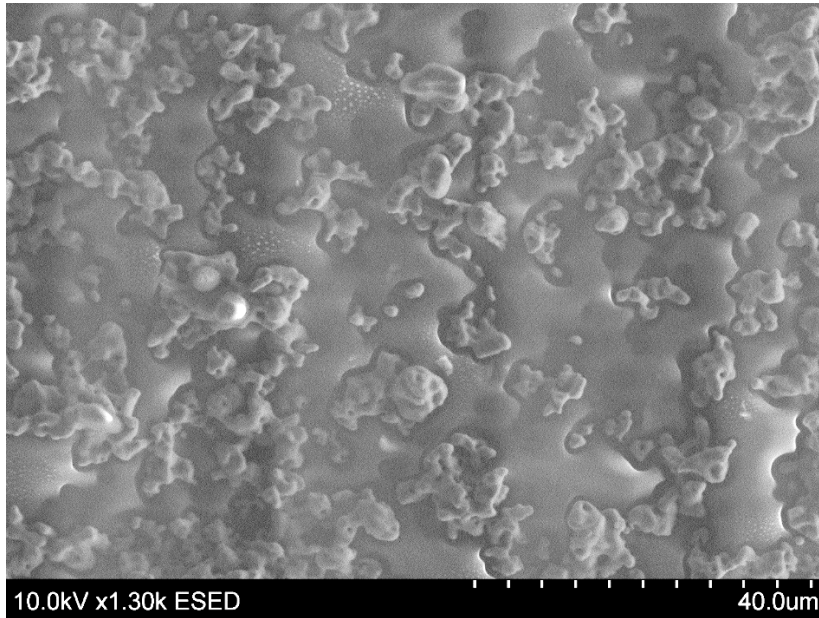
Sample 3 Mass Loss – 9.92mg / cm² (exposure area), 4.42 mg/cm² (total area)

Sample 4 Mass Loss – Adhered to graphite holder

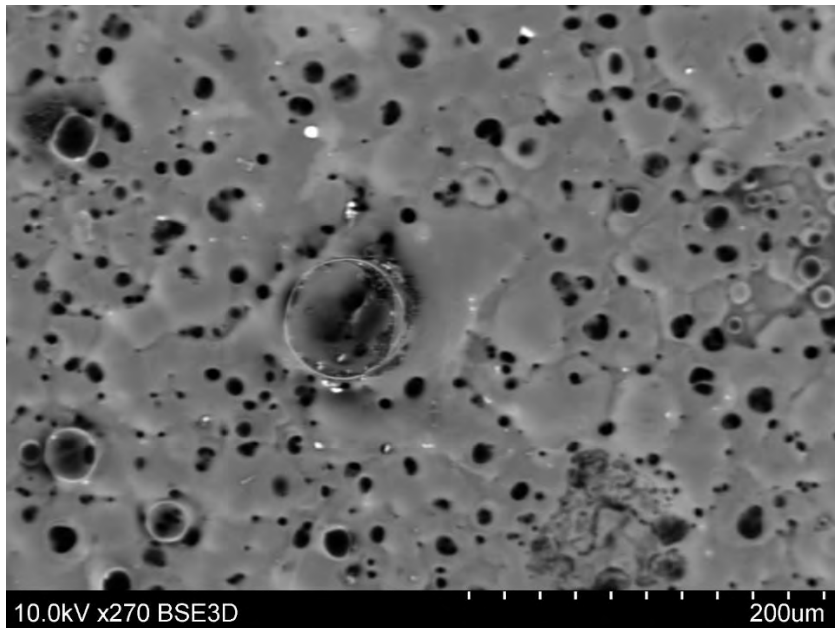
Images for Sample 2 are shown below. The unexposed side shows a pore free surface with several faceted features on the surface. Molybdenum distribution, by EDS, is uneven throughout the surface showing no

preference for faceted features or the darker regions in between. The exposed side shows a porous structure with the aforementioned faceted features no longer present.

Sample 2 – Unexposed Surface – ESED



Sample 2 – Exposed Surface – 3D BSE



III.4 Characterization of Oxyacetylene Torch Flow Conditions

Oxyacetylene Torch Freestream Optical Spectroscopy Gas Characterization:

Emission spectra were collected at 1cm, 2cm, and 4cm from the torch tip for an oxygen to fuel volumetric flowrate ratio (VFR) of 1.5. The spectra showed the presence of the C₂ swan band system with peaks at 438nm, 516nm, 563nm, and 619nm. CH emission peaks at 390 and 430nm and an OH peak at 306nm were also detected. The intensity of the CH and C₂ peaks decreased steadily with increasing position from the torch tip as seen in Fig. 26. The observation of C-based compounds indicates incomplete combustion of the flame up to 2cm away from the nozzle. The intensity of the OH peak at 306 nm, however, increased temporarily before decreasing as the distance from the torch tip was increased. From previous studies on oxyacetylene torch characterization, it is known that as you increase distance from the nozzle, the flame begins to take in oxygen from the surroundings.

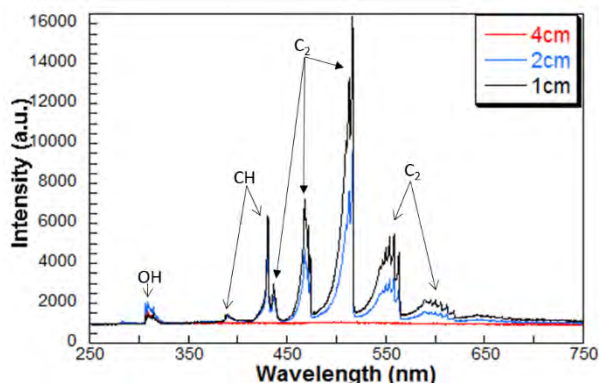


Figure 26: Emission spectrum of the free stream with a 1.5 VFR.

Optical Spectroscopic Analysis of Graphite (polycrystalline) and UHTC Composites:

The emission spectra collected from the graphite sample is shown in Fig. 27. The graph for graphite shows data collection in the visible range as the graphite heats and glows; the graphite sample holder measured a maximum temperature of 2150°C. Two distinct peaks are seen in the broad spectrum at 589nm and 769nm. The 589nm peak corresponds to excited diatomic nitrogen (N₂) and the 769nm peak is an oxygen triplet. This background spectrum is used to provide a reference for the UHTC spectral data. The emission spectra collected from the ZrB₂ and ZrB₂-25SiC samples are shown in Fig. 28(a). Maximum temperatures for ZrB₂ and ZrB₂-SiC are 2000°C and 2100°C, respectively. ZrB₂ sample emissions showed three distinct peaks at 493nm, 518nm, and 547nm that correspond to boron oxides. The presence of these peaks is due to the oxidation and volatilization of the species during testing. The intensity of these peaks decreases significantly with added SiC content most likely due to the higher stability of a borosilica glass mixture that is known to inhibit material loss during oxidation. Figure 28(b) focuses on the region 400-600nm to show the very minor humps of boron oxide in ZrB₂-25SiC. In the same region, it was expected to see SiO volatile species, but due to the oxygen pressure in the flame, the silicon oxide may be stable as SiO₂ liquid.

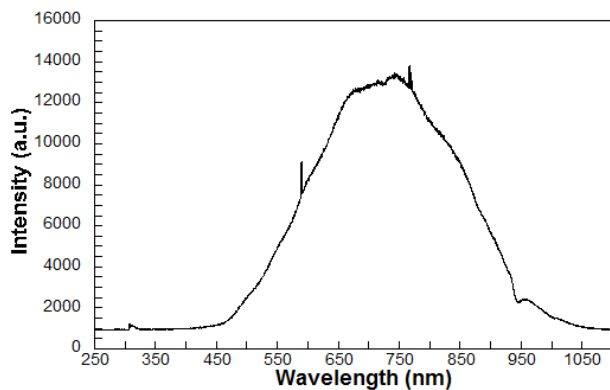


Figure 27: Emission spectrum for a graphite polycrystalline solid.

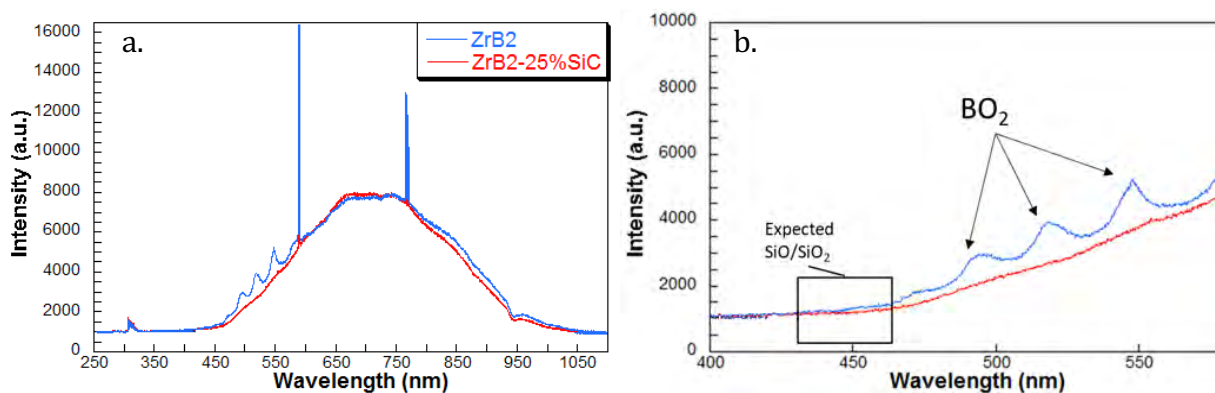


Figure 28: (a) Emission spectrum for ZrB_2 and $ZrB_2-25SiC$, and (b) a focused graph on the volatile boron species for the two materials.

List of Publications and Presentations

Publications:

K.S. Prata, T.E. Schwartzentruber, and T.K. Minton, "Air-Carbon Ablation Model for Hypersonic Flight from Molecular Beam Data", in preparation for submission to *Carbon*, June 2020.

L. Liu, C. Shi, C. Zhang, J.H. Perepezko, "Effect of Al addition on oxidation behavior of a new Mo-Si-B alloy" in preparation, June 2020.

Murray, J. J.; Recio, P.; Caracciolo, A.; Miossec, C.; Balucani, N.; Casavecchia, P.; Minton, T. K. "Oxidation and Nitridation of Vitreous Carbon at High Temperatures", *Carbon* 2020. DOI: 10.1016/j.carbon.2020.05.076.

Murray, Vanessa J., and Timothy K. Minton. "Gas-surface interactions of atomic nitrogen with vitreous carbon." *Carbon* 150 (2019): 85-92.

V.J. Murray, E.J. Smoll, Jr., and T.K. Minton, "Dynamics of Graphite Oxidation at High Temperature," *J. Phys. Chem. C* 2018, DOI: 10.1021/acs.jpcc.7b11772.

L Liu, C Shi, C Zhang, PM Voyles, JH Fournelle, JH Perepezko, "Microstructure, microhardness and oxidation behavior of Mo-Si-B alloys in the $Mo_{ss} + Mo_2B + Mo_5SiB_2$ three phase region" *Intermetallics* 116, 106618 (2020)

L. Liu, C. Sun, C. Zhang, P. Voyles, J. Fournelle, A. Handt, and J.H. Perepezko, "Examination of B in the Mo solid solution (Mo_{ss}) in $Mo_{ss} + Mo_5SiB_2 + Mo_2B$ alloys", *Scripta Materialia* 163 (2019) pp. 62-65.

D. Pham, J.H. Dycus, J.M. LeBeau, M. Venkateswara, K. Muralidharan, and E.L. Corral, "Thermochemical Model on the Carbothermal Reduction of Oxides During Spark Plasma Sintering of Zirconium Diboride," Special Section: International Conference on Sintering, *Journal of the American Ceramic Society*, **102** [2] 757-767 (2018). doi.org/10.1111/jace.15911 Selected as one of the top 15 papers published in the Journal of the American Ceramic Society for 2018 out of over 1,000 articles published.

J.H. Perepezko, "The Effect of Borosilica Pack-Cementation Coatings on the Oxidation Resistance of Mo-Si-B Based Alloys", TMS Annual Meeting & Exhibition, 2017.

L. Liu and J.H. Perepezko, "Mechanical Behavior of Mo Solid Solutions with Minor B and Si Additions", *Materials Science & Technology*, 2019.

J.H. Perepezko, "Phase Stability in Refractory Metal Silicides," *Materials Science & Technology*, 2019.

L. Liu and J.H. Perepezko, "Microstructure, microhardness and oxidation behavior of Mo-Si-B alloys in the $Mo_{ss} + Mo_2B + Mo_5SiB_2$ three phase region", TMS Annual Meeting & Exhibition, 2020.

Achambath, A.D., Ramjatan, S., and Schwartzentruber, T.E., "Surface Properties on Thermal Protection System Microstructure during Hypersonic Ablation", AIAA Paper 2019-1283, presented at the AIAA Aerospace Sciences Meeting, SciTech Forum, San Diego, CA.

"Gas-Surface Interactions with sp^2 Carbon in Extreme Environments," Vanessa J. Murray, Ph.D. Thesis, Department of Chemistry and Biochemistry, Montana State University, May 2018. Winner of the Department's Pagenkopf Award for Outstanding Graduate Research.

A.D. Achambath, and T.E. Schwartzentruber, "Molecular Simulation of Boundary Layer Flow over Thermal Protection System Microstructure", *AIAA Paper 2018-0493*, presented at the AIAA Aerospace Sciences Meeting, SciTech Forum, Kissimmee, FL.

Student Poster Presentations:

Poster: Prata, K.S., and Schwartzentruber, T.E., “Finite-rate air-carbon ablation model”, presented at the 11th Ablation Workshop, Sept. 16-17, 2019, Minneapolis, MN.

Poster: Ramjatan, S. and Schwartzentruber, T.E., “DSMC Simulation of Flow Over Various TPS Microstructures”, 10th Ablation Workshop, Sept. 17-18, 2018, Vermont.

Poster: Prata, K.S. and Schwartzentruber, T.E., “CFD Modeling of Subsonic Plasma Flow for Ablation Experiments”, 10th Ablation Workshop, Sept. 17-18, 2018, Vermont.

Poster: “Dynamics of Graphite Oxidation at High Temperature,” V. J. Murray, E. J. Smoll, Jr., P. J. Woodburn, and T. K. Minton, *Dynamics of Molecular Collisions XXVI*, Granlibakken Conference Center, Tahoe City, CA, July 9-14, 2017.

→ [Award for Best Poster to Vanessa J. Murray]

Poster: “Dynamics of Graphite Oxidation at High Temperature,” V. J. Murray, E. J. Smoll, Jr., P. J. Woodburn, and T. K. Minton, *Gordon Research Conference on Dynamics at Surfaces*, Salve Regina University, Newport, RI, July 30 – August 4, 2017.

→ [Award for Best Poster to Vanessa J. Murray]

Poster: “Dynamics of Graphite Oxidation at High Temperature,” V. J. Murray, E. J. Smoll, Jr., P. J. Woodburn, and T. K. Minton, *9th Ablation Workshop*, Montana State University, Bozeman, MT, August 30-31, 2017.

Poster: “Molecular Simulation of Boundary Layer Flow over Thermal Protection System Microstructure”, Achambath, A.-D. and Schwartzentruber, T.E., *9th Ablation Workshop*, Aug. 30-31, 2017, Bozeman, MT.

Invited and Contributed Talks:

Schwartzentruber, T.E., “Finite-rate modeling of reactions between dissociated air and carbon at high temperature”, presented at the 11th Ablation Workshop, Sept. 16-17, 2019, Minneapolis, MN.

T. K. Minton, “Studies of Gas-Surface Collisions Applied to Space Technology,” Smead Department of Aerospace Engineering Sciences, University of Colorado, Boulder, CO, January 23, 2020.

T. K. Minton, “Molecular Beam Studies of Carbon and Silicon Carbide Ablation by Atomic Oxygen,” Spectral Energies, Dayton, OH, March 29, 2019.

T. K. Minton, “Molecular Beam Studies of Carbon Ablation by O and N atoms,” *11th Ablation Workshop*, University of Minnesota, Minneapolis, Minnesota, September 16-17, 2019.

T. K. Minton, “Molecular Beam Studies of Carbon and Silicon Carbide Ablation by Atomic Oxygen,” *2nd Applied Space Environments Conference*, Los Angeles, CA, May 12-17, 2019.

T. K. Minton, “Studies of Gas-Surface Interactions Applied to Space Technology,” Department of Mechanical Engineering, University of Kentucky, Lexington, KY, February 21, 2019.

T.K. Minton “Molecular Beam Studies of Carbon and Silicon Carbide Ablation by Atomic Oxygen,” *10th Ablation Workshop*, University of Vermont, Burlington, VT, September 17-18, 2018.

E.L. Corral “*Oxidation Behavior of Ultra High Temperature Aerospace Materials in High Enthalpy Flows Using an Oxyacetylene Torch Facility*,” Mechanical and Aerospace Engineering Department, University of California-San Diego, San Diego, CA, February 5, 2018.

E.L. Corral “*Oxidation Behavior of Ultra High Temperature Aerospace Materials in High Enthalpy Flows Using an Oxyacetylene Torch Facility*,” Materials Science and Engineering Department, University of California-Davis, Davis, CA, March 22, 2018.

E.L. Corral “*Oxidation Behavior of Ultra High Temperature Aerospace Materials in High Enthalpy Flows Using an Oxyacetylene Torch Facility*,” Mechanical and Aerospace Engineering Department, University of Kentucky, Lexington, KY, April 13, 2018.

E.L. Corral “*Oxidation Behavior of Ultra High Temperature Aerospace Materials in High Enthalpy Flows Using an Oxyacetylene Torch Facility*,” Aerosciences Department, Sandia National Laboratories, Albuquerque, NM, April 6, 2018.

E.L. Corral “*Oxidation Behavior of Ultra High Temperature Aerospace Materials in High Enthalpy Flows Using an Oxyacetylene Torch Facility*,” Ceramic Materials and Processes, Composites Branch, Materials and Manufacturing Directorate, Air Force Research Laboratory, Wright-Patterson Air Force Base, OH, April 21, 2018.

E. Corral, “*A thermochemical model for oxidation of ultra-high temperature ceramics using high temperature high enthalpy and high temperature flows*,” 10th Ablation Workshop, University of Vermont, Burlington, VT, September 17- 18, 2018.

“Dynamics of Energetic Gas-Surface Interactions,” T. K. Minton, Department of Chemistry, BYU-Idaho, Rexburg, Idaho, April 27, 2017.

“Fundamental Studies of Material Response in Atmospheric Entry Environments,” T. K. Minton, *Applied Space Environments Conference*, Huntsville, Alabama, May 15-19, 2017.

“Dynamics of O-Atom Collisions on Hot Carbon Surfaces,” T. K. Minton, Department of Chemistry, Fudan University, Shanghai, China, October 12, 2017.

“Dynamics of Carbon Oxidation at High Temperatures,” S. J. Poovathingal, V. J. Murray, M. Qian, B. C. Marshall, P. J. Woodburn, E. J. Smoll Jr., T. K. Minton, *9th Ablation Workshop*, Montana State University, Bozeman, MT, August 30-31, 2017.

“Ablation of Graphitic Materials in the Diffusion-Controlled Regime using Dynamic Non-Equilibrium Thermogravimetric Analysis,” E. Corral, *9th Ablation Workshop*, Montana State University, Bozeman, MT, August 30-September 1, 2017.

“Nonequilibrium Gas-Surface Interactions at High Temperature,” T.E. Schwartzentruber, *9th Ablation Workshop*, Montana State University, Bozeman, MT, August 30-September 1, 2017.

Special Session on “Experimental Measurements of Gas-Surface Interactions for Hypersonic Flows”, organized by Schwartzentruber at AIAA SciTech 2018:

“Molecular Beam Scattering Studies of Carbon Oxidation at High Temperatures,” T. K. Minton, *AIAA Scitech Forum*, Kissimmee, FL, January 8-12, 2018.

“Behavior of Ultra High Temperature Aerospace Materials in High Enthalpy Flows Using an Oxyacetylene Torch Facility,” E. Corral, *AIAA Scitech Forum*, Kissimmee, FL, January 8-12, 2018.

REFERENCES:

- [1] Park, C., "Effects of atomic oxygen on graphite ablation," *AIAA Journal*, Vol. 14, No. 11, 1976, pp. 1640–1642. <https://doi.org/10.2514/3.7267>.
- [2] Park, C., and Bogdanoff, D. W., "Shock-Tube Measurement of Nitridation Coefficient of Solid Carbon," *Journal of Thermophysics and Heat Transfer*, Vol. 20, No. 3, 2006, pp. 487–492. doi:10.2514/1.15743
- [3] L. Zhang, D. A. Pejakovic, J. Marschall, M. Dougherty, D. Fletcher, Laboratory investigation of the active nitridation of graphite by atomic nitrogen, *Journal of Thermophysics and Heat Transfer* 26 (1) (2012) 10–21
- [4] Suzuki, T., Fujita, K., and Sakai, T., "Graphite Nitridation in Lower Surface Temperature Regime," *Journal of Thermophysics and Heat Transfer*, Vol. 24, No. 1, 2010, pp. 212–215. doi:10.2514/1.43265
- [5] Goldstein, H. W., "The Reaction of Active Nitrogen with Graphite," *Journal of Physical Chemistry*, Vol. 68, No. 1, 1964, pp. 39–42. doi:10.1021/j100783a007
- [6] Zhluktov, S. V., and Abe, T., "Viscous Shock-Layer Simulation of Airflow past Ablating Blunt Body with Carbon Surface," *Journal of Thermophysics and Heat Transfer*, Vol. 13, No. 1, 1999, pp. 50–59. <https://doi.org/10.2514/2.6400>.
- [7] Havstad, M. A., and Ferencz, R. M., "Comparison of Surface Chemical Kinetic Models for Ablative Reentry of Graphite," *Journal of Thermophysics and Heat Transfer*, Vol. 16, No. 4, 2002, pp. 508–515. <https://doi.org/10.2514/2.6725>.
- [8] Wool, M. R., "Passive Noretip Technology (PANT) Program," *Acurex Corp., Aerotherm Division Final Summary*, June 1975, pp. Rept. 75–159.
- [9] MacLean, M., Marschall, J., and Driver, D., "Finite-Rate surface chemistry model, II: Coupling to viscous navier-stokes code," *42nd AIAA Thermophysics Conference*, 2011, p. 3784.
- [10] Lewis, S. W., Morgan, R. G., McIntyre, T. J., Alba, C. R., and Greendyke, R. B., "Expansion Tunnel Experiments of Earth Reentry Flow with Surface Ablation," *Journal of Spacecraft and Rockets*, Vol. 53, No. 5, 2016, pp. 887–899. <https://doi.org/10.2514/1.A33267>.
- [11] Lewis, S. W., Morgan, R. G., McIntyre, T. J., Alba, C., and Greendyke, R. B., "Comparison of Carbon Ablative Shock-Layer Radiation with High Surface Temperatures," *45th AIAA Thermophysics Conference*, 2015, p. 2348.
- [12] Alba, C. R., Greendyke, R. B., Lewis, S. W., Morgan, R. G., and McIntyre, T. J., "Numerical Modeling of Earth Reentry Flow with Surface Ablation," *Journal of Spacecraft and Rockets*, Vol. 53, No. 1, 2016, pp. 84–97. <https://doi.org/10.2514/1.A33266>.
- [13] Alba, C. R., Greendyke, R. B., and Marschall, J., "Development of a Nonequilibrium Finite-Rate Ablation Model for Radiating Earth Reentry Flows," *Journal of Spacecraft and Rockets*, Vol. 53, No. 1, 2016, pp. 98–120. <https://doi.org/10.2514/1.A33303>.
- [14] Murray, V. J., Marshall, B. C., Woodburn, P. J., and Minton, T. K., "Inelastic and reactive scattering dynamics of hyperthermal O and O₂ on hot vitreous carbon surfaces," *The Journal of Physical Chemistry C*, Vol. 119, No. 26, 2015, pp. 14780–14796.
- [15] Garton, D. J., Brunsvold, A. L., Minton, T. K., Troya, D., Maiti, B., and Schatz, G. C., "Experimental and theoretical investigations of the inelastic and reactive scattering dynamics of O (3 P) + D₂," *The Journal of Physical Chemistry A*, Vol. 110, No. 4, 2006, pp. 1327–1341.
- [16] Zhang, J., Garton, D. J., and Minton, T. K., "Reactive and inelastic scattering dynamics of hyperthermal oxygen atoms on a saturated hydrocarbon surface," *The Journal of Chemical Physics*, Vol. 117, No. 13, 2002, pp. 6239–6251. <https://doi.org/10.1063/1.1460858>.
- [17] Murray, V. J., and Minton, T. K., "Gas-surface interactions of atomic nitrogen with vitreous carbon," *Carbon*, Vol. 150, 2019, pp. 85–92.
- [18] Murray, V. J., Smoll Jr, E. J., and Minton, T. K., "Dynamics of graphite oxidation at high temperature," *J. Phys. Chem.*, Vol. 122, No. 12, 2018, pp. 6602–6617.

- [19] Poovathingal,S.J., Qian,M., Murray,V.J., and Minton,T.K., “Reactive and Scattering Dynamics of Hyperthermal O and O₂ from a Carbon Fiber Network,” <https://scholarworks.montana.edu/xmlui/handle/1/14696>, 2018.
- [20] Poovathingal, S., Schwartzentruber, T. E., Murray, V. J., and Minton, T. K., “Molecular Simulation of Carbon Ablation Using Beam Experiments and Resolved Microstructure,” *AIAA Journal*, Vol. 54, No. 3, 2016, pp. 999–1010. <https://doi.org/10.2514/1.J054562>.
- [21] Poovathingal,S., Schwartzentruber,T.E., Murray,V.J., Minton,T.K., and Candler,G.V., “Finite-rate oxidation model for carbon surfaces from molecular beam experiments,” *AIAA journal*, 2017, pp. 1644–1658.
- [22] Swaminathan-Gopalan, K., Borner, A., Murray, V. J., Poovathingal, S., Minton, T. K., Mansour, N., and Stephani, K. A., “Development and validation of a finite-rate model for carbon oxidation by atomic oxygen,” *Carbon*, Vol. 137, 2018, pp. 313–332.
- [23] Swaminathan-Gopalan,K., and Stephani, K.A., “Construction of finite rate surface chemistry models from pulsed hyperthermal beam experimental data,” *AIP Advances*, Vol. 9, 2019, p. 035246.
- [24] Murray, J. J.; Recio, P.; Caracciolo, A.; Miossec, C.; Balucani, N.; Casavecchia, P.; Minton, T. K. Oxidation and Nitridation of Vitreous Carbon at High Temperatures. *Carbon* 2020. DOI: 10.1016/j.carbon.2020.05.076.
- [25] Edel,R., Grabnic,T., Wiggins,B., and Sibener,S.J., “Atomically-Resolved Oxidative Erosion and Ablation of Basal Plane HOPG Graphite Using Supersonic Beams of O₂ with Scanning Tunneling Microscopy Visualization,” *The Journal of Physical Chemistry C*, Vol. 122, No. 26, 2018, pp. 14706–14713.
- [26] Rosner, D., and Allendorf, H., “High temperature oxidation of carbon by atomic oxygen,” *Carbon*, Vol. 3, No. 2, 1965, pp. 153–156.
- [27] Olander,D. ,Jones,R., Schwarz,J., and Siekhaus,W., “Reactions of Modulated Molecular Beams with Pyrolytic Graphite: II. Oxidation of the Prism Plane,” *J. Chem. Phys*, Vol. 57, 1972, p. 421.
- [28] Lutz, “Experimental Investigation And Analysis Of High-Enthalpy Nitrogen Flow Over Graphite,” PhD Thesis, University of Vermont.
- [29] Helber, B., Turchi, A., and Magin, T. E., “Determination of active nitridation reaction efficiency of graphite in inductively coupled plasma flows,” *Carbon*, Vol. 125, 2017, pp. 582–594.
- [30] K.S. Prata, T. E. Schwartzentruber, and T. K. Minton, “Air-Carbon Ablation Model for Hypersonic Flight from Molecular Beam Data”, manuscript in preparation for submission to Carbon, June 2020.
- [31] Helber, Chazot, Hubin, and Magin, “Microstructure and gas-surface interaction studies of a low-density carbon-bonded carbon fiber composite in atmospheric entry plasmas”, *Composites Part A: Applied Science and Manufacturing* 72 (2015) pp. 96-107.
- [32] F. Gai, M. Miller-Oana, V.R. Manga, M. Packard, L.S. Walker, E.L. Corral, A comparative study on oxidation behavior of various graphitic microstructures using thermogravimetric analyses, *Carbon Prep. Submiss.* (2020).
- [33] E.L. Corral, R.E. Loehman, Ultra-High-Temperature Ceramic Coatings for Oxidation Protection of Carbon–Carbon Composites, *J. Am. Ceram. Soc.* 91 (2008) 1495–1502. <https://doi.org/10.1111/j.1551-2916.2008.02331.x>.
- [34] D.E. Rosner, H.D. Allendor, Comparative studies of the attack of pyrolytic and isotropic graphite by atomic and molecular oxygen at high temperatures., *AIAA J.* 6 (1968) 650–654. <https://doi.org/10.2514/3.4558>.
- [35] M. Levy, P. Wong, The Oxidation of Pyrolytic Graphite at Temperatures of 1400~176 and at Air Velocities of 2S-100 cm/sec, *J. Electrochem. Soc.* 111 (n.d.) 4.
- [36] F. Stevens, L.A. Kolodny, T.P. Beebe, Kinetics of Graphite Oxidation: Monolayer and Multilayer Etch Pits in HOPG Studied by STM, *J. Phys. Chem. B.* 102 (1998) 10799–10804. <https://doi.org/10.1021/jp982025e>.
- [37] J.R. Hahn, Kinetic study of graphite oxidation along two lattice directions, *Carbon.* 43 (2005) 1506–1511. <https://doi.org/10.1016/j.carbon.2005.01.032>.

- [38] H. Chang, A.J. Bard, Scanning tunneling microscopy studies of carbon-oxygen reactions on highly oriented pyrolytic graphite, *J. Am. Chem. Soc.* 113 (1991) 5588–5596. <https://doi.org/10.1021/ja00015a012>.
- [39] P.L. Walker Jr., F. Rusinko Jr., L.G. Austin, Gas Reactions of Carbon, in: P.W.S. and P.B.W. D.D. Eley (Ed.), *Adv. Catal.*, Academic Press, 1959: pp. 133–221. <http://www.sciencedirect.com/science/article/pii/S0360056408604186> (accessed November 18, 2016).
- [40] M. Rossberg, Experimentelle Ergebnisse über die Primärreaktionen bei der Kohlenstoffverbrennung, *Z. Für Elektrochem. Berichte Bunsenges. Für Phys. Chem.* 60 (1956) 952–956. <https://doi.org/10.1002/bbpc.19560600905>.
- [41] N.S. Jacobson, D.M. Curry, Oxidation microstructure studies of reinforced carbon/carbon, *Carbon*. 44 (2006) 1142–1150. <https://doi.org/10.1016/j.carbon.2005.11.013>.
- [42] D.W. McKee, Oxidation behavior of matrix-inhibited carbon/carbon composites, *Carbon*. 26 (1988) 659–664. [https://doi.org/10.1016/0008-6223\(88\)90068-1](https://doi.org/10.1016/0008-6223(88)90068-1).
- [43] Panerai, F., Helber, B., Chazot, O., and Balat-Pichelin, M., “Surface temperature jump beyond active oxidation of carbon/silicon carbide composites in extreme aerothermal conditions”, *Carbon*, 71, pp. 102-119 (2014).
- [44] Presser, V. and Nickel, K. G., “Silica on silicon carbide”, *Critical Reviews in Solid State and Materials Sciences*, Vol. 33, No. 1, 2008, pp. 1-99.
- [45] H. Hald, “Operational limits for reusable space transportation systems due to physical boundaries of c/sic materials”, *Aerospace Science and Technology*, Vol. 7, (7), 551–559, 2003.
- [46] G. Herdrich, M. Fertig, S. Löhle, S. Pidan, and M. Auweter-Kurtz, “Oxidation behavior of siliconcarbide-based materials by using new probe techniques”, *Journal of Spacecraft and Rockets*, Vol. 42, No. 5, pp 817–824, 2005.
- [47] I. Sakraker, C. Asma, and F. Panerai, “Experimental study on the passive-active oxidation transition of the fast 20XX spaceliner thermal protection system”, 4th European Conference for Aero-Space Sciences (EUCASS), San Petersburg, Russia, 2011.
- [48] B. Helber, F. Panerai, O. Chazot, and M. Balat-Pichelin, “Reusability limits of carbon/silicon carbide heat shield materials - Part 2: Volatilization detection by space- and time-resolved emission spectroscopy”, *Specialists Meeting on “Catalytic Gas Surface Interactions*, Educational Notes RTO-EN-AVT-199, Rhode-Saint-Genèse, Belgium, 2012.
- [49] Balat-Pichelin, M., Charpentier, L., Panerai, F., Chazot, O., Helber, B., and Nickel, K., “Passive/active oxidation transition for CMC structural materials designed for the IXV vehicle re-entry phase”, *Journal of the European Ceramic Society*, Vol. 35 (2015) 487-502.
- [50] M. Gasch, D. Ellerby, E. Irby, S. Beckman, M. Gusman, and S. Johnson, “Processing, properties, and arc jet oxidation of hafnium diboride/silicon carbide ultra high temperature ceramics”, *Journal of Materials Science*, Vol. 39, (19), 5925–5937, 2004.
- [51] D. Glass, “Physical challenges and limitations confronting the use of UHTCs on hypersonic vehicles”, *AIAA International Space Planes and Hypersonic Systems and Technologies Conference*, AIAA Paper 2011-2304, San Francisco, CA, 2011.
- [52] J. Marschall, D. Pejaković, W. Fahrenholtz, G. Hilmas, F. Panerai, and O. Chazot, “Temperature jump phenomenon during plasmatron testing of ZrB₂-SiC ultrahigh-temperature ceramics”, *Journal of Thermophysics and Heat Transfer*, Vol. 26, No. 4, 2012.
- [53] D. M. Dimiduk and J. H. Perepezko. Mo-Si-B alloys: Developing a revolutionary turbine-engine material. *Mrs Bulletin* 28 (2003): 639-645.
- [54] J. H. Perepezko. The hotter the engine, the better. *Science* 326 (2009): 1068-1069.
- [55] W. O. Soboyejo, and T. S. Srivatsan, eds. *Advanced structural materials: properties, design optimization, and applications*. CRC press, 2006.
- [56] P. Jain, and K. S. Kumar. Tensile creep of Mo–Si–B alloys. *Acta Materialia* 58 (2010): 2124-2142.

- [57] S. Burk, G. Bronislava, and C. Hans-Jürgen. High temperature oxidation of Mo–Si–B alloys: effect of low and very low oxygen partial pressures. *Acta Materialia* 58 (2010): 6154-6165.
- [58] P. Jain, and K. S. Kumar. Dissolved Si in Mo and its effects on the properties of Mo–Si–B alloys. *Scripta Materialia* 62 (2010): 1-4.
- [59] H. Nowotny, R. Kieffer, and F. Benesovsky. Silicoboride der Übergangsmetalle Vanadin, Niob, Tantal, Molybdän und Wolfram (Silicoborides of the transition metals vanadium, niobium, tantalum, molybdenum and tungsten). *Planseeber Pulvermetall* 5 (1957): 86-93.
- [60] H. Nowotny, E. Dimakopoulou, and H. Kudielka. Untersuchungen in den Dreistoffsystemen: Molybdän-Silizium-Bor, Wolfram-Silizium-Bor und in dem System: VSi 2– TaSi 2. *Monatshefte für Chemie/Chemical Monthly* 88.2 (1957): 180-192.
- [61] R. Sakidja, J. H. Perepezko, S. Kim, and N. Sekido. Phase stability and structural defects in high-temperature Mo–Si–B alloys. *Acta Materialia*, 56 (2008): 5223-5244.
- [62] R. Sakidja, and J. H. Perepezko. Phase stability and alloying behavior in the Mo-Si-B system. *Metallurgical and Materials Transactions A* 36 (2005): 507-514.
- [63] S. Kim, and J. H. Perepezko. Interdiffusion kinetics in the Mo₅SiB₂ (T₂) phase. *Journal of phase equilibria and diffusion* 27 (2006): 605-613.
- [64] R. Sakidja, and J. H. Perepezko. Alloying and microstructure stability in the high-temperature Mo–Si–B system. *Journal of Nuclear Materials* 366 (2007): 407-416.2
- [65] N. Sekido, R. Sakidja, and J. H. Perepezko. Annealing response of point defects in off-stoichiometric Mo₅SiB₂ phase. *Intermetallics* 15 (2007): 1268-1276.
- [66] F. A. Rioult, S. D. Imhoff, R. Sakidja, and J. H. Perepezko. Transient oxidation of Mo–Si–B alloys: effect of the microstructure size scale. *Acta Materialia* 57 (2009): 4600-4613.
- [67] Y. Ying, H. Bei, S. Chen, E. P. George, J. Tiley, and Y. A. Chang. Effects of Ti, Zr, and Hf on the phase stability of Mo_{ss}+Mo₃Si+Mo₅SiB₂ alloys at 1600° C. *Acta Materialia* 58 (2010): 541-548.
- [68] Y. Yang, Y. A. Chang, L. Tan, and Y. Du. Experimental investigation and thermodynamic descriptions of the Mo–Si–Ti system. *Materials Science and Engineering: A* 361 (2003): 281-293.
- [69] Y. Yang, and Y. A. Chang. Thermodynamic modeling of the Mo–Si–B system. *Intermetallics* 13 (2005): 121-128.
- [70] Y. Yang, Y. A. Chang, L. Tan, and W. Cao. Multiphase equilibria in the metal-rich region of the Mo–Ti–Si–B system: thermodynamic prediction and experimental validation. *Acta Materialia* 53 (2005): 1711-1720.
- [71] G. Hasemann, D. Kaplunenko, I. Bogomol, and M. Krüger. Near-Eutectic Ternary Mo-Si-B Alloys: Microstructures and Creep Properties. *JOM* 68 (2016): 2847-2853.
- [72] M. Heilmaier, M. Krüger, H. Saage, J. Rösler, D. Mukherji, U. Glatzel, and R. Völkl. Metallic materials for structural applications beyond nickel-based superalloys. *JOM* 61(2009): 61-67.
- [73] Pandat. Software package for multi-component phase diagram calculation, developed by CompuTherm LLC, 437 S. Yellowstone Dr., Madison, WI 53719, USA; 1999
- [74] J. A. Lemberg, and R. O. Ritchie. Mo-Si-B Alloys for Ultrahigh - Temperature Structural Applications. *Advanced Materials* 24 (2012): 3445-3480.
- [75] L. Liu, C. Sun, C. Zhang, P.M. Voyles, J. Fournelle, A. Handt and J. H Perepezko. Examination of B in the Mo solid solution (Moss) in Moss + Mo₅SiB₂ + Mo₂B alloys. *Scripta Materialia*, 163 (2019): 62-65.